NORMAL MODES IN NORTH ATLANTIC ATMOSPHERE-OCEAN SYSTEM AND PREDICTING NORTH ATLANTIC SEA SURFACE TEMPERATURE

by

Bowen Zhao

A thesis submitted to the faculty of
The University of Utah
in partial fulfillment of the requirements for the degree of

Master of Science

Department of Atmospheric Sciences

The University of Utah

August 2016

The University of Utah Graduate School

STATEMENT OF THESIS APPROVAL

The thesis of **Bowen Zhao**

has been approved by the following supervisory committee members:

Courtenay Strong	, Chair	**04/19/2016** Date Approved
Timothy J. Garrett	, Member	**04/19/2016** Date Approved
Matthew Newman	, Member	**04/19/2016** Date Approved

and by **Kevin Perry** , Chair/Dean of

the Department/College/School of **Atmospheric Sciences**

and by David B. Kieda, Dean of The Graduate School.

ABSTRACT

We identify an interdecadal oscillatory mode of the North Atlantic atmosphere-ocean system via a Linear Inverse Model (LIM). This mode is shown to be related to the interior pathway propagation of Atlantic Meridional Overturning Circulation (AMOC) anomalies. The oscillation is an ocean-only mode while excited by atmospheric forcing; in particular, it can be approximated as a linearly driven damped oscillator while the North Atlantic Oscillation (NAO) acts as part of the "external" force. We also show that the influence of NAO-induced surface wind stress forcing quickly damps while the NAO-induced deep flow anomaly, integrating with ocean topography, plays a crucial role in this interdecadal mode. Including such deep ocean dynamics besides surface temperature (SST) significantly improves and prolongs the LIM's prediction skill of SST evolution.

CONTENTS

LIST OF FIGURES

Figures Page

LIST OF TABLES

ACKNOWLEDGMENTS

First, I thank Dr. Thomas Reichler and Dr. Courtenay Strong for advising me during my master's study in the University of Utah. Also, I very much appreciate all professors who inspired and encouraged my dedication to science, especially Professor Tim Garrett, Professor Elena Cherkaev and Professor James Keener. Thanks to Cécile Penland and Matt Newman, who provide guides for understanding LIM and other help.

I thank my parents for always sharing my happiness and sadness and for being my refuge and my strength. Thanks to Xingxing and Jingyuan who warm my heart with friendship. Thanks to Dien, Shixuan, Zhen, Chao and all others for making life easier here.

CHAPTER 1

INTRODUCTION

Sea surface temperature (SST) is characteristic of the interface between two fluids of different viscosity and heat capacity and hence is exposed to influences of both fast atmospheric variations and slow oceanic variations. On the other hand, the oceanic variability is largely influenced by the atmosphere through buoyancy and momentum fluxes, and further could probably feed back onto the atmosphere [1]. Ignoring other climate components, this is already an interesting coupled system with SST sensitively detecting the interactions between the atmosphere and the ocean. One aim of this study is to build a simple model that is capable of describing SST variations and reflecting the above ideas.

The first order approximation for SST variation, laid by Hasselmann [2], is a red noise model that incorporates atmospheric white noise through the ocean's larger heat capacity. Since then, many studies have sought additional mechanisms to account for SST interannaul or interdecadal variability. Both the "coupled atmosphere-ocean oscillatory mode" hypothesis [3, 4, 5] and the "ocean-only mode excited by atmosphere forcing" proposition [6] include ocean current advection as a major factor for SST variability on these timescales. The North Atlantic, with both horizontal gyre circulation and meridional overturning circulation (AMOC), thus has become a focus of these studies and also of the present study.

During the last decade, enormous effort has been directed at investigating North Atlantic ocean circulation variation, particularly the impact of atmospheric forcing on ocean circulation, for example, the relationship between the North Atlantic Oscillation (NAO) (or its variation, the East Atlantic Pattern) and the AMOC or the subpolar gyre [7, 8, 9, 10]. However, there still lacks a unifying understanding about the interdecadal variation of the North Atlantic atmosphere-ocean system either in nature or in global climate models (GCMs). On the other hand, some recent studies [11, 12, 13] emphasize the role of ocean topography, via bottom vortex stretching, in explaining the mean and variation of the North Atlantic ocean circulation and provide alternative explanatory mechanisms besides

the classical wind stress forcing perspective. In this paper, we employ an inverse method (Linear Inverse Model, LIM) to study the North Atlantic atmosphere-ocean system in a 4000-year-long control run from the Geophysical Fluid Dynamics Laboratory CM2.1 model (GFDL CM2.1) [14]. Inverse methods have the advantage of extracting signals without requiring prior knowledge or hypotheses; however, we need to rely on established propositions to explain the patterns and signals obtained, and hence LIM can also play the role of examining existing hypotheses.

This study is not the first one to invoke LIM to study the North Atlantic climate system. Tziperman et al. [15] constructed LIM from 3D temperature and salinity field of a general circulation model (GFDL CM2.1) to study the possibility of transient amplification of modest initial perturbation via nonnormal interference, as a follow up of previous works based on a simple box model [16] and a zonally averaged model [17]. Hawkins and Sutton [18] also examined the predictability and optimal perturbations of the Atlantic ocean with LIM but in a different GCM (HadCM3). Zanna [19] and Vimont [20] also constructed LIM but from SST observations to study Atlantic SST predictability. While these studies already demonstrated LIM's validity in studying the Atlantic atmosphere-ocean system and provided some insight into the North Atlantic climate variation through examining variance growth, this study will focus on revealing physical mechanisms of the interdecadal variation in the North Atlantic atmosphere-ocean system. From this perspective, this study is more similar to Sevellec and Fedorov [21] except that we do not directly linearize GCM equations, only to fit a linear system in some optimal sense.

This thesis is organized as follows. In Chapter 2, we briefly introduce LIM and our other methods. In Chapter 3, we show main results from this study: In section 3.1, we show prediction skill of LIM constructed in various ways and discuss the implications; In section 3.2, we focus on the dominant interdecadal normal mode and address bottom vortex stretching theory to interpret it; In section 3.3, we summarize the North Atlantic atmosphere-ocean system using spectral analysis. The conclusion is presented in Chapter 4.

CHAPTER 2

METHODOLOGY AND DATA

2.1 Methodology

As mentioned above, instead of directly linearzing the full GCM equations (i.e. the tangent linear model approach), we fit a linear model to the North Atlantic atmosphere-ocean system, that is, we employ the "linear inverse modelling" (LIM) method. If fitted properly, as we shall show below, LIM can not only capture the linearized part of the full dynamics as the tangent linear model does, but also gives statistical properties of the nonlinear part. The essence of LIM is based on scale separation: if nonlinearites decorrelate quickly enough, then their effect on slow processes of interest can be approximated as stochastic noise according to the "Central Limit Theorem"; further assume the slow processes are mostly linear, then the system can be well described by [22]

$$\frac{d\boldsymbol{X}}{dt} = \boldsymbol{L}\boldsymbol{X} + \boldsymbol{\xi}, \tag{2.1}$$

where $\boldsymbol{X}$ is the state variable, including all relevant processes we are interested in, and $\boldsymbol{\xi}$ is the noise vector. It has been known for long that there indeed is a separation of timescale in the atmosphere-ocean system. For example, by taking the annual mean of our data, almost all atmospheric processes and most oceanic eddy processes would go to the stochastic noise part $\boldsymbol{\xi}$ while the linearizable advection would be left in the linear dynamics part and described by $\boldsymbol{L}$.

The operator matrix $\boldsymbol{L}$ can be determined from covariance statistics as

$$\exp(\boldsymbol{L}\tau) = \boldsymbol{C}(\tau)\boldsymbol{C}(0)^{-1}, \tag{2.2}$$

where $\boldsymbol{C}(\tau)$ is the covariance matrix for lag τ. The covariance matrix of the LIM system would then evolve as

$$\boldsymbol{C}(\tau) = \exp(\boldsymbol{L}\tau)\boldsymbol{C}(0), \tag{2.3}$$

which, compared with the covariance matrix for lag τ from observation or GCMs, could be used as a test for the LIM. The noise covariance matrix $\boldsymbol{Q} = \langle \boldsymbol{\xi}\boldsymbol{\xi}^T \rangle dt$ can be determined

from the fluctuation-dissipation relationship

$$\boldsymbol{L}\boldsymbol{C}(0) + \boldsymbol{C}(0)\boldsymbol{L}^T + \boldsymbol{Q} = 0. \tag{2.4}$$

The first several eigenvectors of $\boldsymbol{Q}$ tell the dominant noise patterns. Note that the noise term $\boldsymbol{\xi}$ is white in time but not in space as fast processes can have large spatial scales. After $\boldsymbol{L}$ and $\boldsymbol{Q}$ have been derived from data, we can then integrate EQ.2.1 to make forecasts [23]:

$$\hat{\boldsymbol{X}}(t + \triangle t) = (\boldsymbol{I} + \boldsymbol{L}\triangle t)\hat{\boldsymbol{X}}(t) + \triangle t/2)\boldsymbol{S}\boldsymbol{r}(t)$$
$$X(t + \triangle t2) = (\hat{\boldsymbol{x}}(t) + \hat{\boldsymbol{x}}(t + \triangle t))/2$$

where $\boldsymbol{I}$ is the identity matrix, S is a constant matrix related with $\boldsymbol{Q}$ ($\boldsymbol{Q} = \boldsymbol{S}\boldsymbol{S}^T$) and $\boldsymbol{r}$ is a vector of independent Gaussian variables.

If LIM constructed as above shows high consistency with the original system it is intended to approximate, one can hope that both the dominant linear dynamics and the noise statistics approximate well the slow and fast processes in the original system. The degree of consistency can be measured by cross-validated forecast skill, following Newman et al. [24]. The cross-validated skill is calculated as such: subsample the data by removing a 400-year segment while fitting the LIM to the remaining data, make forecasts for removed years and repeat this process for all years. The cross-validated forecast skill is then defined as the correlations between forecasts and the original data.

The dynamics of the linear system can be revealed by applying eigen-decomposition to the operator $\boldsymbol{L}$, whose eigenvectors $\boldsymbol{u}_i$ give Principal Oscillation Patterns [25] or Empirical Normal Modes (hereafter normal modes) [22], while corresponding eigenvalues $\lambda = \zeta + \eta i$ give exponential decaying times ($-\frac{1}{\zeta}$) and characteristic periods ($\frac{2\pi}{\eta}$). If no eigenvalues are degenerate, $\boldsymbol{X}$ can then be uniquely represented as the linear combination of $\boldsymbol{u}_i$s, that is, normal modes act as the basis of the system

$$\boldsymbol{X} = \boldsymbol{U}\boldsymbol{d}(t), \tag{2.5}$$

where the ith column of $\boldsymbol{U}$ is the normal mode $\boldsymbol{u}_i$ while the ith row $d_i(t)$ of $\boldsymbol{d}(t)$ is the corresponding coefficients. Modes that have a longer decay timescale will dominate over modes that decay quickly, if equally excited by noise, and manifest themselves in the summation of all modes, namely $\boldsymbol{X}$ time series. This is why less damped eigenmodes attract more attention. $\boldsymbol{d}(t)$ can then be obtained by projecting $\boldsymbol{X}$ onto $\boldsymbol{U}^{-1}$ in matrix space while

the common practice is to invoke adjoint patterns $\boldsymbol{V}$, whose columns $\boldsymbol{v}_i$s are eigenvectors of the conjugate transpose of $\boldsymbol{L}$, $\boldsymbol{L}^H$, as $\boldsymbol{U}$ and $\boldsymbol{V}$ form a biorthogonal set

$$\boldsymbol{U}^H\boldsymbol{V} = \boldsymbol{U}\boldsymbol{V}^H = \boldsymbol{I}, \tag{2.6}$$

where $\boldsymbol{I}$ is the identity matrix. Making use of the biorthogonality,

$$\boldsymbol{d}(t) = \boldsymbol{V}^H\boldsymbol{X}. \tag{2.7}$$

The adjoint pattern $\boldsymbol{v}_i$ has the biggest normalized covariant projection onto $\boldsymbol{u}_i$ and hence tells the sensitivity of corresponding normal modes $\boldsymbol{u}_i$. To reveal related signals in variable $\boldsymbol{Y}$ fields that are not included in constructing the LIM, we calculate the so-called "associated correlation pattern" $\boldsymbol{v}_i$ as the regression of $y(t)$ onto $d_i(t)$ [25]

$$\boldsymbol{Y}(t) = \sum_i d_i(t)\boldsymbol{q}_i + \boldsymbol{e}(t), \tag{2.8}$$

where the error $\boldsymbol{e}(t)$ is to be minimized.

$$\boldsymbol{q}_i = \sum_k \boldsymbol{D}^{-1}_{k,l}\langle d^{l*}y\rangle, \tag{2.9}$$

where $\boldsymbol{D}$ is the covariance matrix

$$\boldsymbol{D}_{k,l} = \langle d^{k*}d^l\rangle. \tag{2.10}$$

When we restrict to one dominant normal mode,

$$\boldsymbol{q} = \frac{\langle|d|^2\rangle\langle d^*\boldsymbol{Y}\rangle - \langle d^{*2}\rangle\langle d\boldsymbol{Y}\rangle}{\langle d^*d\rangle^2 - \langle d^2\rangle\langle d^{*2}\rangle}. \tag{2.11}$$

Storch et al. [26] demonstrated that normal modes extracted from observations can capture the most unstable mode derived from conventional stability analysis. LIM has also been demonstrated to be successful in predicting and investigating ENSO [22, 24] and extratropical troposphere variability [27]. As mentioned above, several studies have employed LIM to gain some insight about the North Atlantic atmosphere-ocean system with the focus on predictability and transient amplification.

Besides LIM, we also examine spectral properties of two kinds of oscillator: a linearly driven, damped oscillator and a negative delayed oscillator, which are two main conceptual

prototypes for atmosphere-ocean coupling proposed by Griffies and Tziperman [6] and Battisti and Hirst [28], respectively. The linearly driven oscillator x can be described by

$$\ddot{x} + \gamma\dot{x} + \omega_0^2 x = f = \sum_{\omega} F(\omega)\cos(\omega t), \tag{2.12}$$

where f is stochastic white forcing and $F(\omega)$ its Fourier coefficients. The phase lag ϕ between oscillator x and force f is then [29]

$$\tan\phi(\omega) = \frac{-\gamma\omega}{\omega_0^2 - \omega^2}. \tag{2.13}$$

The amplitude of the oscillator (A) varies as

$$A(\omega) = \frac{F(\omega)}{\sqrt{(\omega_0^2 - \omega^2)^2 + \gamma^2\omega^2}}. \tag{2.14}$$

As to the delayed oscillator, we adopt the separated form as in Sun et al. [30]

$$c\dot{x} = a\hat{f} - x/b$$
$$\hat{f}(t+\tau) = x(t),$$

where x denotes sea surface temperature (SST) or other oceanic variables and $\hat{f}$ denotes atmospheric forcing, c is the heat capacity, a is the forcing strength, b is x's memory timescale and τ is the delay time between x and $\hat{f}$.

Last, all spectral results shown are derived from using the Multi-taper Method (MTM) [31] and further smoothed in frequency domain. Significance levels for coherency are decided from a F-test while those for spectra are determined from a red noise null hypothesis and a χ^2-test.

2.2 Data

In this study, we use a 4000-year-long GFDL CM2.1 pre-industrial control run. The atmosphere component has a resolution of $2^\circ \times 2.5^\circ$ with 24 vertical levels. The ocean component has a horizontal resolution of $1^\circ \times 1^\circ$, which becomes progressively finer approaching the equator while the resolution at the equator is $1/3^\circ$. There are 50 levels vertically, 22 of which are evenly spaced within the top 220 m. All data used in this study are annual mean anomalies. Also, as our conclusions are not noticeably influenced by the trend present in the data, we did not detrend in any sense. The training lag to compute $\boldsymbol{L}$ from Eq. 2.2 is 1 year. The state variable $\boldsymbol{X}$ includes SST, barotropic streamfunction and meridional streamfunction defined for the region [25°N, 65°N; 80°W, 20°E], with Hudson

Bay and Mediterranean Sea masked for oceanic variables. Note that SST is defined here as surface temperature above sea ice when sea ice is present, and adopting temperature below sea ice does not change our conclusions. We do not explicitly include atmospheric variables into $\boldsymbol{X}$ as taking annual mean makes atmospheric variables mostly behave like the stochastic noise according to the Central Limit Theorem, which can deteriorate $\boldsymbol{L}$ when included in $\boldsymbol{X}$. The salinity information is surely important for the North Atlantic ocean but velocity field should already include the effect of salinity and hence we do not expect dramatic changes in our conclusions when we further include salinity. Nevertheless, without salinity data, we may have difficulty in attributing causes and we will consider salinity in our future study. To illustrate oceanic dynamics, we also calculate associated correlation patterns for the upper and lower level vertically integrated v-velocity (hereafter up VIV and bot VIV, respectively), separating at 2000 m (changing this depth to 1200 m affects results minimally).

To exclude possibly nonlinear, small-scale processes, SST data and u,v data for barotropic streamfunction computation are first interpolated to a 4×4 degree grid. v velocity data for computing meridional streamfunction are not smoothed in any sense. Because various fields with different units are involved, each anomaly field is normalized by its domain-averaged climatological root-mean square amplitude. To reduce the dimension of the system, we then project data onto the EOF space and truncate to retain only the first several Principal Components (PCs) and hence $\boldsymbol{X}$ includes the first several PCs of SST, barotropic streamfunction and meridional streamfunction. To facilitate interpretation, we present results transformed back from EOF to grid space. Here we show results retaining 9, 8 and 9 EOFs for SST, barotropic streamfunction and meridional streamfunction, which explain 85%, 83% and 97% of total variance, respectively. As shown in Fig. 2.1, this combination is decided from maximizing SST variance explained by LIM's predictions. The prediction explained variance is defined as the domain averaged cross-validated correlation skill squared. The computation process is as such: first, for a fixed SST PC number included in $\boldsymbol{X}$, we search for barotropic and meridional streamfunction PC numbers that maximize the SST explained variance by prediction at five years in advance and record the maximum explained variance; then we increase the SST PC number included in $\boldsymbol{X}$ until the maximum explained variance stops increasing. Fig. 2.1d shows some oscillation, causing some ambiguity in deciding which PC number combination to choose. However, we find that the two extrema yield basically the same dominant normal modes and we only present results for the [9,8,9] combination case. Note that for small SST PC numbers as only 3 are included, the prediction skill

is not remarkably worse than including many more SST PCs. This already suggests the importance of including oceanic current information to make good SST predictions.

In examining the role of atmosphere in the North Atlantic atmosphere-ocean system, we particularly look at the North Atlantic Oscillation (NAO), defined as the first empirical orthogonal function (EOF) of sea level pressure over the region of [20°N,80°N; 90°W,40°E]. We also use a Atlantic Meriodional Overturning Circulation (AMOC) strength index, defined as the maximum meridional streamfunction at 45°N (denoted as 45°AMOC).

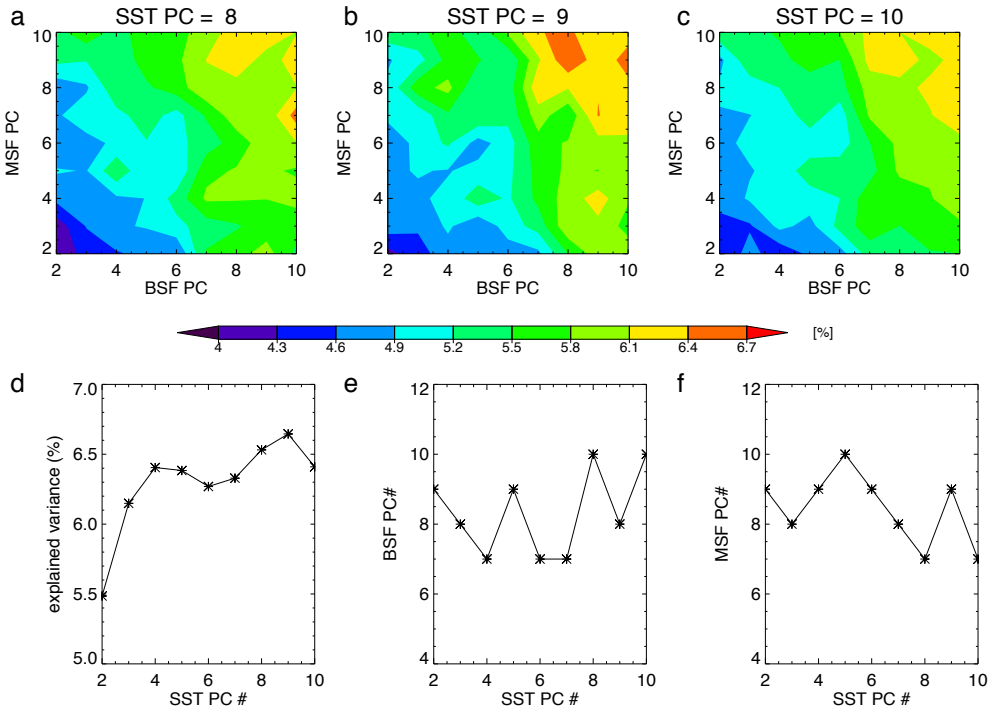

Figure 2.1. SST's prediction explained variance vary with PC numbers of SST, barotropic streamfunction and meridional streamfunction included in $\boldsymbol{X}$. Note that prediction explained variance is calculated for prediction at 5-year lead time. (a-c) Variation of prediction explained variance with respect to barotropic and meridional streamfunction PC numbers for fixed SST PC number, the SST PC number is shown above each plot. The maximum value in each plot is denoted by maximum explained variance. (d) Variation of maximum explained variance with respect to SST PC number changes. (e) Barotropic streamfunction PC numbers corresponding to maximum explained variance. (f) Meridional streamfunction PC numbers corresponding to maximum explained variance.

CHAPTER 3

RESULTS

3.1 How Well Does LIM Represent GCM Dynamics

As argued above, SST receives influence from both above and below and thus serves as a critical test for approximations of the North Atlantic atmosphere-ocean system, so here we focus on examining the SST prediction skill to see how well LIM represents the system. In Fig. 3.1, we show the prediction skill of North Atlantic SST by our LIM and by an AR-1 model, along with the differences between them, at 5-year lead time. The increase in skill of LIM relative to AR-1 is remarkable in the subpolar gyre region, arguing for the validity of our linear approximation there. Note that Zanna [19] examined SST's prediction skill by LIM constructed from SST only and found that the prediction skill is worst in the subpolar gyre region and much better in the subtropic North Atlantic. As we shall see later, the differences in prediction skill for the subpolar gyre region results from the fact that we explicitly include oceanic current information into LIM while the differences in prediction skill for the subtropic North Atlantic is probably due to that our domain does not include equatorial and south Atlantic, which are expected to modulate midlatitude SST. We also note that the increase in skill does not vary monotonically with lag but reaches a maximum at around 5-year lead time (Fig. 3.1d), which suggests that it is the inclusion of relatively low-frequency information, probably ocean dynamics, that contributes to the skill improvement. We explore this conjecture by comparing with a different LIM constructed from SST only (referred to as SST-LIM). The fact that the oscillation in lagged auto-covariance of North Atlantic SST is better captured by LIM than by SST-LIM (Fig. 3.2) confirms that including ocean dynamics, contained in the barotropic and meridional streamfunction part of $\mathbf{X}$, allows LIM to capture the interdecadal variability in SST and make better long-term predictions. The success of LIM in predicting SST evolution and the SST auto-covariance pattern thus allows us to further investigate the underlying oceanic dynamics. As implied by Fig. 3.2a, SST shows maximum variances in the region of [40°N, 65°N; 80°W, 30°W]; later we will focus on comparing SST averaged in this region between

GCM and LIM, denoting these time series as SST-index.

3.2 Normal Modes

There are a total of 26 normal modes generated from this LIM, 10 of which are complex modes. As normal modes summed together should be equal to $\boldsymbol{X}$, which is real, complex normal modes have to come as complex conjugate pairs. Thus we combine complex conjugate pairs together and count them as one mode. While complex normal modes represent oscillatory modes, real ones represent monotonically exponential decaying modes. The least damped mode has a decay time of ∼23 years (Table 3.1), which is very different from the slow decay timescale of 1200 years in Tziperman et al. [15]. This huge difference tells us that the 3D temperature and salinity fields contain much more information than barotropic and meridional streamfunctions do. Table 3.1 lists all normal modes and their contributions to SST-index variations and 45° AMOC variations. Note that at least the first 5 least damped modes all contribute much to the SST-index and 45° AMOC variations. We also looked at the optimal initial condition as other LIM studies did and find that it projects onto multiple normal modes. These all confirm the idea that the system is nonnormal and that interference among normal modes with difference decay timescales is important [15]. However, as we shall demonstrate later, realizing the importance of nonnormality cannot exclude that a particular normal mode can reveal important physical mechanisms, which is the initial motivation of normal modes [32]. Among these 16 normal modes, we are most interested in Mode 2 not only because it is the least damped oscillatory mode but also because it contributes remarkably to both the SST-index variations and the 45°AMOC variations (with correlation of 0.45 and 0.64, respectively, see Fig. 3.3b and h), revealing the role of deep ocean in SST variations and possibly implying atmosphere-ocean coupling. The associated eigenvalue suggests Mode 2 has an estimated period of around 20 years while spectral analysis of the Mode 2 coefficients gives a probable range of 15-25 years (the mode period corresponds to the frequency at which the real and imaginary part of the mode coefficient both have large power and are highly coherent while in quadrature).

As this study focuses on interpreting the spatial patterns of Mode 2, it is necessary to show that the Mode 2 patterns are robust. We first test the robustness of Mode 2 against changing the number of EOFs included in $\boldsymbol{X}$. We choose the PC number combinations that maximize LIM's prediction explained variance, i.e. we adopt combinations shown in Fig. 2.1d. Then we calculate spatial correlations between normal modes in those combinations

and normal modes in the [9,8,9] combination. It turns out that up to the first 3 least damped modes, the normal modes are correlated with correlation greater than 0.9 while the critical correlation coefficient for 99% significance level is less than 0.21 depending on the number of grid points. For Mode 2, the decay timescale, period and contributions to SST-index and 45°AMOC also barely change (see Table. 3.2). We also test the robustness of Mode 2 patterns against the data used to construct LIM. As we evenly segment the whole 4000-year data into 4 segments, it turns out that the oscillatory Mode 2 barely changes (Table. 3.3) while monotonic Modes 1 and 3 are more susceptible, with decay timescale and contribution to SST-index and 45°AMOC varying quite much, which may not be surprising considering that the data are not subject to any detrend techniques. Nevertheless, the spatial patterns of the first 3 least damped modes remain mostly unchanged.

Next, we will focus on interpreting the spatial patterns of Mode 2. As shown in Figs. 3.5 and 3.6, this normal mode evolves, from 0° to 270° phase, as $\boldsymbol{\alpha} \to \boldsymbol{\beta} \to -\boldsymbol{\alpha} \to -\boldsymbol{\beta}$, where $\boldsymbol{\alpha}$ and $-\boldsymbol{\beta}$ are real and imaginary parts of the complex normal mode, that is, $c\boldsymbol{u}_2(t)+c^\star\boldsymbol{u}_2^\star(t) = \exp(\zeta t)\cdot(\boldsymbol{\alpha}\cos(\eta t) - \boldsymbol{\beta}\sin(\eta t))$. The normalization parameter c is decided by requiring $\boldsymbol{\alpha}\boldsymbol{\beta} = 0$, $\boldsymbol{\alpha}\boldsymbol{\alpha} = 1$ and $\boldsymbol{\beta}\boldsymbol{\beta} \geq 1$ [22].

We argue that this mode is related to the interior-pathway propagation of high-latitude AMOC anomalies. First we show the regression of barotropic and meridional streamfunctions onto 45°AMOC in Fig. 3.7. Changing the AMOC definition to a different latitude only changes the relative phase but not the evolution sequence. It is obvious that the evolution from lag -5 to +5 years in Fig. 3.7 is consistent with Mode 2 from phase 90° to 270° (e.g. Fig. 3.5d → h and e → i), indicating that Mode 2 is a physically meaningful and important mode in this GCM. The consistency between the regression patterns and Mode 2 patterns also implies that the barotropic and meridional streamfunctions in Mode 2 carry similar information about AMOC anomalies propagation. The consistency is also true for SST and vertically integrated velocity regressed on 45°AMOC (Appendix C). As to the physical interpretation of Mode 2, we refer to the proposition in Zhang [12], who argued that the interior pathway of North Atlantic Deep Water (NADW) in GFDL CM2.1 is not a model artifact but consistent with recent observations [33]. Focusing on half of the cycle, for example, from phase 90° to phase 270°, the barotropic and meridional streamfunction patterns result from the slow equatorward propagation of high-latitude positive AMOC anomalies. First, the meridional streamfunction patterns from Fig. 3.5e → g → i, is a straightforward propagation process of high-latitude positive anomaly. As to the barotropic streamfunction pattern, it is the barotropic vortex response to NADW anomaly. Although

the initial response of barotropic streamfunction to the NADW anomaly is excepted to be a fast Kelvin wave response [34], which induces an anticyclonic gyre along the North American east coast, the majority of NADW anomaly moves along the interior pathway with a slow advection speed [33] and hence we see the cyclonic gyre gradually moves equatorward with a timescale of ∼10 years (see Fig. 3.5d → f →h). As Zhang [12] argued, the interior pathway is downslope from Grand Banks to Cape Hatteras, thus the cyclonic gyre strengthens, due to the bottom vortex stretching, as it moves (also see Fig. 3.5d → f →h). The dominant cooling over the domain and the slight warming southeast of Greenland in the SST pattern (Fig. 3.5e) is clearly advection driven. The cooling confined in the Northern Recirculation Gyre region (NRG) as seen in Fig. 3.5g is also related to the weakening of the Northern Recirculation Gyre and the southward shift of the Gulf Stream [35], which again, results from the cyclonic gyre propagation. We note, however, that the strong warming in the Labrador Sea at phase 270° does not seem to be advection driven and we will come back to this later (defining SST as surface temperature below sea ice only decreases the Labrador Sea temperature anomaly amplitude modestly). The existence of the interior pathway and slow propagation of NADW anomalies is even more clear in the associated correlation patterns of vertically integrated v-velocity (Fig. 3.6). It takes half a period for the initial anomalous southward return flow in the Labrador Sea (Fig. 3.6d) to propagate to southeast of Grand Banks (Fig. 3.6f) and then to the latitude of Cape Hatteras (Fig. 3.6h). Meanwhile the upper ocean North Atlantic Current (NAC) anomaly strengthens from phase 90° (Fig. 3.6c) to phase 180° (Fig. 3.6e). As stated above, the same processes can be seen in the regression plots at higher temporal resolution (Fig. 3.7 and Fig. B1). Note that differences between our regression results and those in Zhang [12] are due to different definitions of the AMOC index since both studies are based on the same model. We thus emphasize the role of ocean topography, which significantly modifies the Kelvin wave propagation mechanism and also interacts with oceanic current via bottom vortex stretching. As Zhang (2010) argued, since the NADW and AMOC anomalies move with mean flow speed north of 35°N, there is a significant lag between subpolar and subtropical AMOC anomalies and may lead to long-term predictability.

However, we are still left with important questions: what completes the cycle and causes the oscillation? Correspondingly, what sets the oscillation period? Zhang [12] pointed out that the weakened mixed layer depth after positive AMOC anomalies propagating southward could induce an anticyclonic gyre in the subpolar gyre region (Fig. 3.5h), which then would initiate the second half of the cycle as the subpolar anticyclonic gyre propagates

southward. The associated correlation pattern for mixed layer depth (Fig. 3.8g) is consistent with this conjecture. This process, if true, makes the existence of an ocean-only mode possible. However, without external factor, this ocean-only mode would eventually die out, thus requiring additional explanatory mechanisms. There are two major propositions in the literature: one is that the ocean-only oscillator is driven by atmospheric forcing [6]; the other is that the cycle is completed by a SST feedback onto the atmosphere [5, 3]. In Marshall et al. [5], the key factor is a dipole pattern of SST anomalies that straddle the polar jet and oppose the climatological SST gradient. However, in Fig. 3.5g we do not see a clear SSTA dipole straddling around 45°N and hence no direct evidence for a "coupled atmosphere-ocean mode." As to Griffies and Tziperman [6], their ocean-only oscillator results from the critical balance between a negative temperature advection feedback and a positive salinity advection feedback while atmospheric noise induces temperature anomalies and drives the damped oscillator. Our results suggest a different mechanism for the ocean-only oscillator but the idea that atmospheric noise drives the ocean-only oscillator seems to agree in both studies. We noticed that in Mode 2, there is a strong SST anomaly in the Labrador Sea (Fig. 3.5c) accompanying high-latitude AMOC anomalies (Fig. 3.5e), which suggests an influence of the NAO. The associated correlation pattern of sea level pressure (Fig. 3.8d) also suggests the involvement of the NAO. Due to the difficult of directly including atmosphere into LIM, we cannot clearly distinguish cause and effect and exclude the possibility of atmosphere-ocean coupled oscillator. Therefore, in the next section, we will examine the role of atmosphere, represented by the NAO, and the nature of this oscillation using spectral analysis.

Before we proceed, let us go back to the nonnormality effect. As Tziperman et al. [15] realized the importance of modal interference in explaining thermohaline circulation anomaly growth, they conclude that it seems improper to interpret the thermohaline circulation or AMOC as a simple harmonic oscillator. However, as noted above, normal modes extracted in our study are very different from those extracted in their study. Mode 2 in this study is the second least damped mode and hence gains more importance than the interdecadal oscillatory mode in their study. The optimal growth, in our case, starts with cancellation among many normal modes as in their study but ends with a pattern heavily projecting onto Mode 2, which is not the case in their study. Therefore, the contrasting conclusions based on the same GCM is due to the fact that these two studies use different variables to construct LIM and hence examine different subsystems of the North Atlantic atmosphere-ocean system. Also, both Hawkins and Sutton [18] and Tziperman et al. [15] point out the importance of temperature/salinity anomaly in the Labrador Sea and Nordic

Sea. As we will show below, we agree with the importance of temperature anomaly in the Labrador Sea. Due to the current limit of our domain and lack of salinity data, we cannot comment on the importance of salinity and the Nordic Sea for now.

3.3 Spectral Analysis and NAO/AMOC Relationship

In this section, we employ a totally independent method, spectral analysis, to provide more insights. As shown in Fig. 3.9d, the coherency between NAO and 45°AMOC is statistically significant at decadal and longer frequencies and the phase lag between 45°AMOC and NAO agrees with that of a linear oscillator x driven by white forcing f (Eq. 2.13, for the determination of parameters see below and Appendix A). The phases based on a delayed oscillator with proper parameters are also shown in Fig. 3.9d (green, red and purple curves correspond to AMOC with memory timescale of 5, 10 and 20 years, respectively; see Appendix B for details) and clearly show less agreement with the phase calculated from GCM. In particular, for the linear oscillator x, the phase lag $\phi(\omega)$ at the natural frequency ω_0 should be -90°, which agrees well with the AMOC-NAO -90° phase lag at the AMOC spectral peak (∼15 years). In light of linear oscillator theory, the spectrum of AMOC (Fig. 3.9e) looks quite similar to the amplitude response of the oscillator x to white forcing f, which reaches its maximum near ω_0. The lag-correlation between AMOC and NAO is also very similar to that between a linear oscillator x and the white forcing f (Fig. 3.9f). The maximum correlation is obtained when the NAO leads the AMOC by approximately one quarter period (-4 years), consistent with a -90° phase lag at resonance. Thus, we are encouraged to interpret the AMOC response to the NAO as that of a linear damped oscillator driven by white forcing rather than a negative delayed oscillator. Spectral results of AMOC and NAO from concatenation of four different GFDL runs of the same length also support this interpretation (Appendix D). Last, we emphasize that the spectral results between NAO and the part of 45°AMOC that comes from Mode 2 alone (Fig. 3.9a-c) agrees with the above interpretation, that is, the phase, coherency, spectrum and correlation between NAO and the part of 45°AMOC that comes from Mode 2 alone agrees with that between NAO and the whole 45°AMOC at intredecadal frequencies. This again supports the idea that the 20-year period oscillation seen in the North Atlantic climate system in this GCM mostly arises from Mode 2. This reproduction is also a very encouraging support for LIM as information about the NAO is only indirectly included in the LIM through the fluctuation-dissipation relationship (Eq. 2.4).

Note that the existence of such a phase function $\phi(\omega)$ indicates that the NAO serves mostly as an "external" force to the AMOC oscillator instead of being an internal component of the oscillator, i.e. the AMOC mode is an ocean-only mode rather than atmosphere-ocean coupled mode. In the context of a linearly driven oscillator, a possible feedback from the AMOC onto the NAO would not change the phase function $\phi(\omega)$, although it would change the spectral power of both AMOC and NAO. This prompts the question of why a white-noise NAO can excite this interdecadal oscillation. Results here indicate that the answer is resonance. The AMOC would respond to the NAO on all frequencies but the response is much higher near the AMOC's natural frequency, which thus exhibits itself in the AMOC time series and the AMOC-NAO lag-correlation. One can show that using Eq. 2.12, the damping coefficient γ and the natural frequency ω_0 can be determined from the AMOC time series and its Hilbert transform (see Appendix A for details). ω_0 determined in this way suggests that the internal period $2\pi/\omega_0 \approx 16$ years and the "AMOC oscillator" is underdamping with $\omega_0/\gamma = 2.6 > 0.5$. Considering the uncertainty, the period estimated from Mode 2 is consistent with the internal period decided here. Actually, the Mode 2 provides a physical explanation for the spectral results: the existence of the interior pathway requires a quarter period to be L/V, which is around 4 years, where L is the distance from Grand Banks to Cape Hatteras and V is mean current velocity [12].

We now regress SST, barotropic streamfunction, meridional streamfunction and vertically integrated v-velocity onto the NAO to show direct evidence of a NAO influence. In Fig. 3.10, the evolution from lag=1 to lag=4 bears similarity with Mode 2 from phase 90° to 180°. Extending the regression to 20 years reveals a full cycle similar to Mode 2 with amplitude decreasing with lag (not shown). However, the lag=0 pattern lacks obvious connection with the patterns at subsequent lags. The SSTs shown in Fig. 3.10a are clearly part of the well-known "Tripolar pattern" (map begins at 25° so only two poles are visible) that results from NAO and its wind stress anomaly-induced turbulent heat flux [36, 37], while Fig. 3.10b resembles the intergyre gyre resulting from NAO-induced wind stress curl, described by Marshall et al. [5]. The dipole in Fig. 3.10c is probably also driven by NAO-related surface wind stress via Ekman drift. In short, the lag=0 pattern is due to the SST and streamfunction response to NAO-induced wind stress anomalies. However, this direct wind stress influence is transient while the influence that projects onto the AMOC is long-lasting. In other words, the mechanism proposed by Marshall et al. [5] seems not active in this GFDL CM2.1 mode, that NAO coupled with the wind stress driven intergyre gyre pattern yields interdecadal oscillation. A last comment would be that NAO regression

pattern at lag=0 is very similar to the dominant noise pattern (defined as the first EOF of noise covariance Q, see Fig. 3.11), suggesting the dominant role of NAO in driving the North Atlantic atmosphere-ocean system.

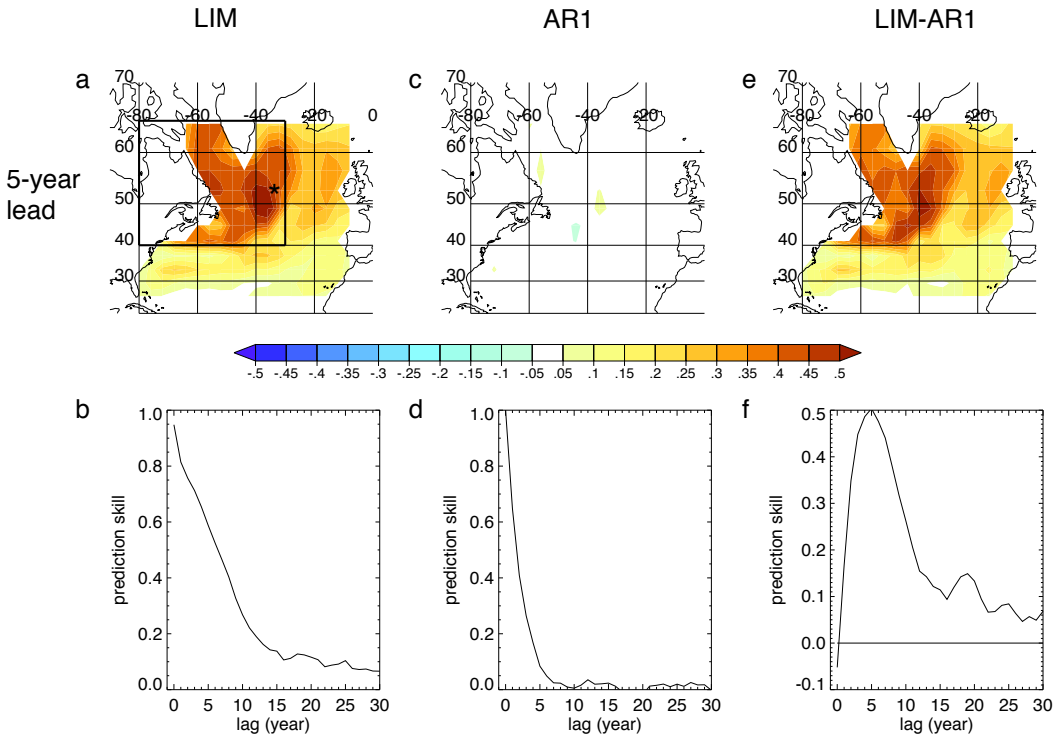

Figure 3.1. Prediction skill. (a-b) Prediction skill for LIM. (c-d) Prediction skill for AR-1 model. (e-f) Prediction skill difference between LIM and AR-1 model. (a), (c) and (e) Prediction skill pattern at 5-year lead time. (b), (d) and (f) Prediction skill for first 30 years in advance at 52°N, 36°W (labeled by $*$ in (a)). Note that in (b) skill is less than 1 at lag = 0-year because we are comparing prediction from truncated EOF space with data from full grid space.

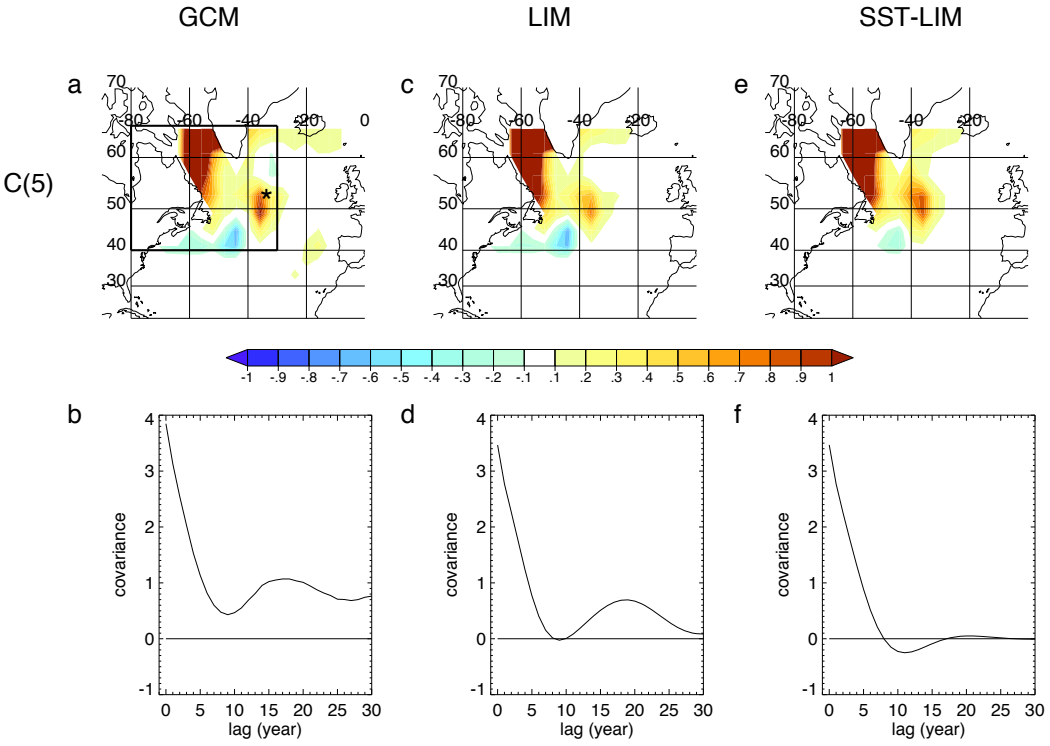

Figure 3.2. Auto-covariance. (a-b) Auto-covariance for GCM. (c-d) Auto-covariance for LIM. (e-f) Auto-covariance for SST-LIM. (a),(c) and (e) Auto-covariance pattern at 5-year lead time. (b), (d) and (f) Auto-covariance for first 30 years at 52°N, 36°W.

Table 3.1. Normal modes are sorted by their exponential decay time. The fourth column is the contribution of each normal mode to the GCM SST-index variations, i.e. SST averaged over [40°N, 65°N; 80°W, 30°W], calculated as correlation between the two. The fifth column is the contribution of each normal mode to the 45°AMOC variations.

Modes	Period (year)	Decay (year)	SST-index correlation	45°AMOC correlation
1	∞	22.76	0.34	0.12
2	20.15	14.32	0.45	0.64
3	∞	7.93	0.39	0.31
4	11.16	5.96	0.35	0.19
5	∞	5.20	0.26	0.29
6	39.04	3.72	-0.03	0.17
7	∞	2.95	-0.11	0.18
8	33.68	1.67	0.06	0.17
9	∞	1.55	0.18	0.02
10	9.03	1.54	0.01	-0.01
11	∞	1.06	0.03	0.05
12	40.30	1.01	0.07	0.01
13	6.52	0.87	0.01	-0.14
14	14.18	0.87	-0.06	0.03
15	12.20	0.81	0.07	0.09
16	27.36	0.55	0.12	0.10

Table 3.2. The least damped oscillatory normal mode from different PC combinations. The first column denotes the PC numbers for SST, barotropic streamfunction and meridional streamfunction. The second to fourth columns are spatial correlations between the least damped oscillatory mode from each PC combination and that from the [9,8,9] combination. The fifth to eighth columns are periods, decay times, contributions to the SST-index and the 45°AMOC variations for each PC combination.

PC numbers	SST cor	BSF cor	MSF cor	Period (year)	Decay (year)	SST-index cor	45°AMOC cor
2,9,9	0.96	0.98	0.99	19.21	14.86	0.42	0.61
3,8,8	-0.96	-1.00	-1.00	20.34	13.67	0.46	0.59
4,7,9	0.97	0.99	1.00	20.57	14.47	0.45	0.61
5,9,10	0.98	0.99	0.99	19.17	15.98	0.44	0.67
6,7,9	0.98	0.99	1.00	20.16	15.03	0.46	0.66
7,7,8	-0.99	-0.99	-1.00	20.12	14.82	0.47	0.67
8,10,7	-0.99	-0.98	-0.99	18.89	15.44	0.44	0.65
9,8,9	1.00	1.00	1.00	20.15	14.32	0.45	0.64
10,10,7	-0.99	-0.98	-0.99	18.93	15.32	0.43	0.65

Table 3.3. The least damped oscillatory normal mode from different segments for the [9,8,9] PC combination. The first column denotes the segment number. The second to fourth columns are spatial correlations between the least damped oscillatory mode from each 1000-year segment and that from the whole 4000-year data. The fifth to eighth columns are periods, decay times, contributions to the SST-index and the 45°AMOC variations for each segment.

segment	SST cor	BSF cor	MSF cor	Period (year)	Decay (year)	SST-index cor	45°AMOC cor
1	-0.96	-0.96	-0.99	20.80	11.69	0.47	0.55
2	-0.99	-0.99	-1.00	21.28	13.77	0.47	0.64
3	0.99	0.99	0.99	19.66	13.21	0.45	0.62
4	0.97	0.98	0.99	18.82	20.09	0.43	0.74
all	1.00	1.00	1.00	20.15	14.32	0.45	0.64

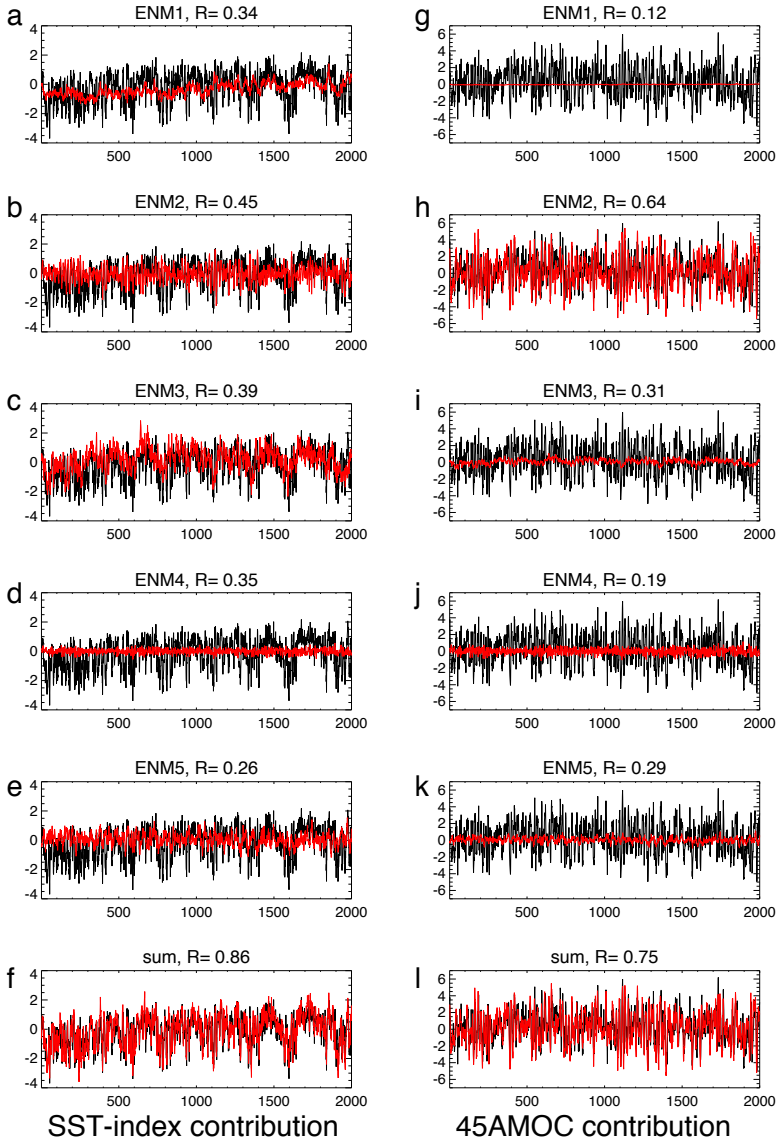

Figure 3.3. Contribution to SST-index and 45°AMOC from first 5 least damped normal modes. Black curves in (a-f) are SST-index from GCM. Red curves in (a-f) are SST-index from Mode 1, Mode 2, Mode 3, Mode 4, Mode 5 and the summation of these modes. (g-k) is same as (a-f) but for 45°AMOC.

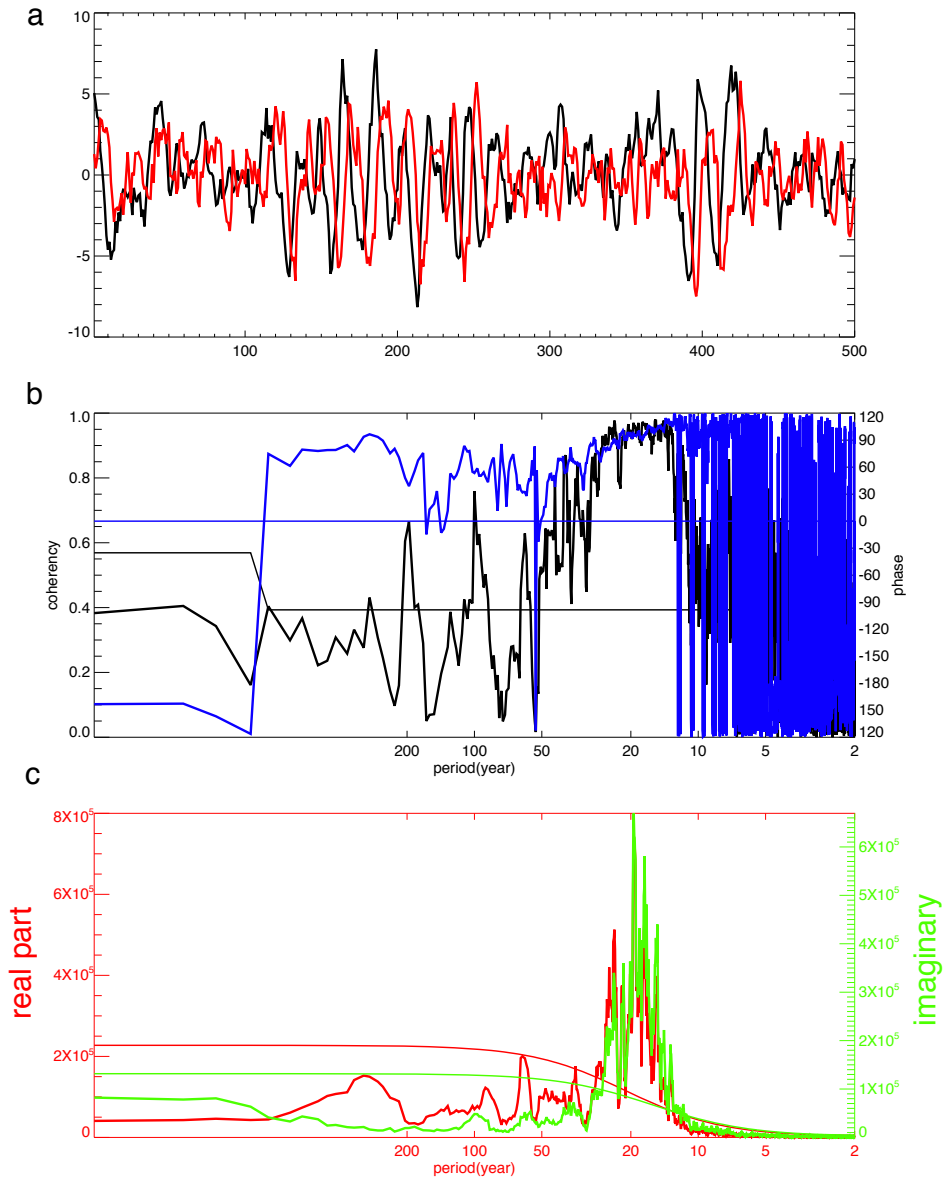

Figure 3.4. Normal Mode 2 coefficient. (a) Black and red curves are real and imaginary parts of normal Mode 2 coefficient $d_2(t)$. (b) Thick black curve is the coherence while thick blue curve is the phase lag between the real and imaginary parts of Mode 2. Thin black curve shows 95% significance level of coherence based on a F-test. (c) Thick red and green curves are spectra of real and imaginary parts of normal Mode 2, respectively. Thin curves with corresponding colors show 95% significance levels based on a red noise null hypothesis and a χ^2-test.

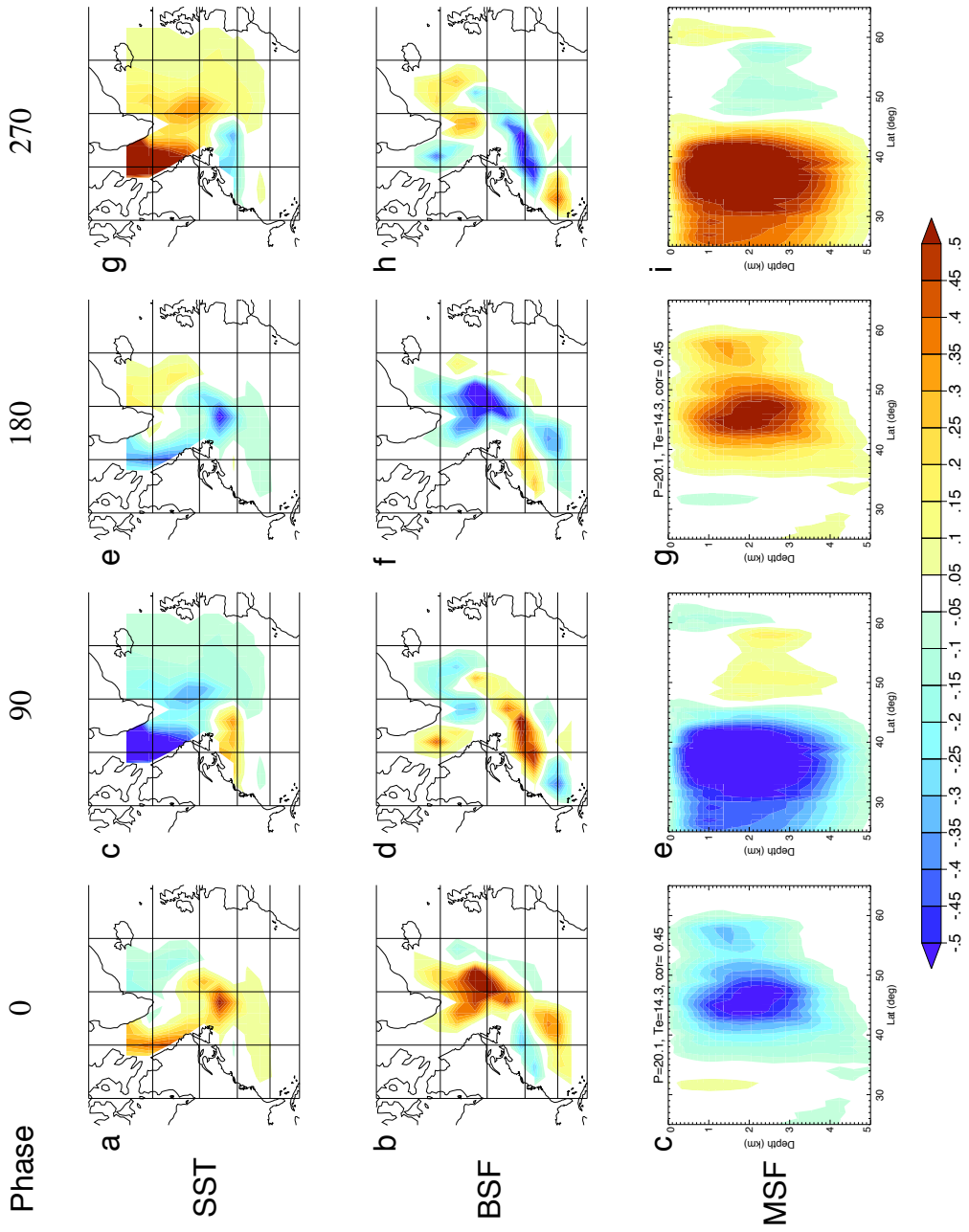

Figure 3.5. Mode 2 spatial pattern. The first row is for SST, the second row is for BSF and the third row is for MSF. The first column is for phase 0° ($\boldsymbol{\alpha}$); the second column is for phase 90° ($\boldsymbol{\beta}$); the third column is for phase 180° ($-\boldsymbol{\alpha}$); the fourth column is for phase 270° ($-\boldsymbol{\beta}$).

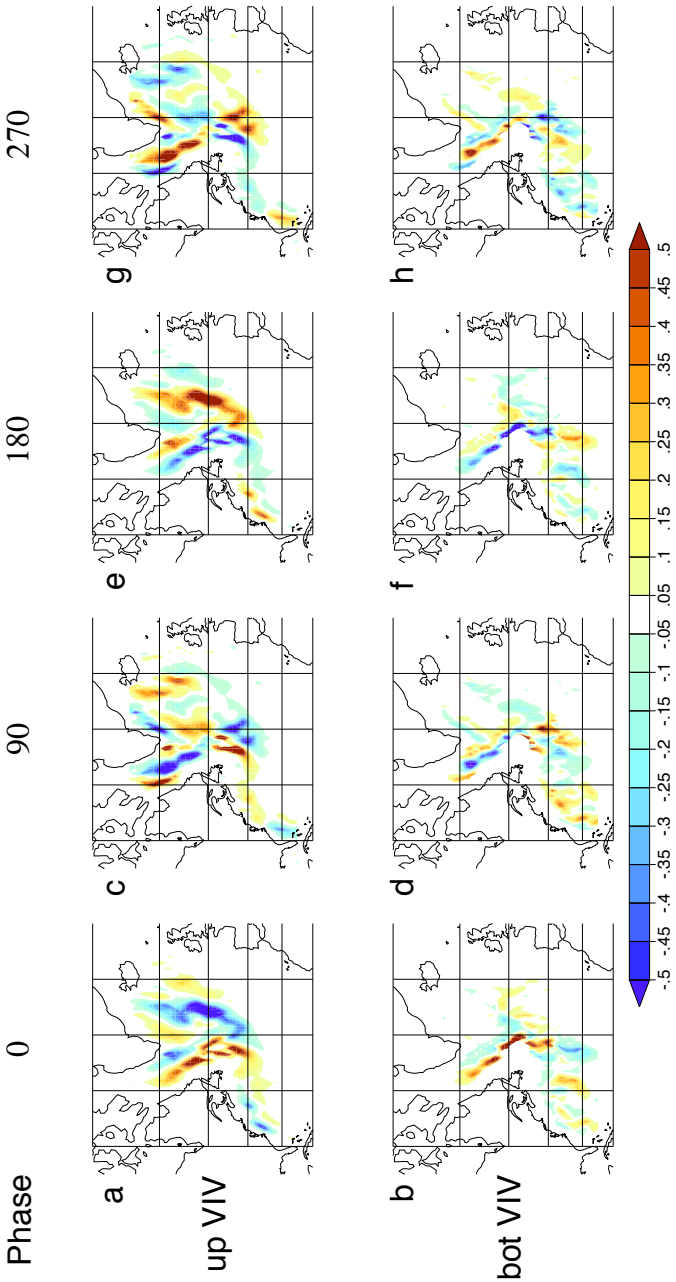

Figure 3.6. Associated correlation pattern (Eq. 2.11) of vertically integrated velocity for Mode 2. The first row is for upper level vertically integrated v-velocity (up VIV), the second row is for lower level vertically integrated v-velocity (bot VIV).

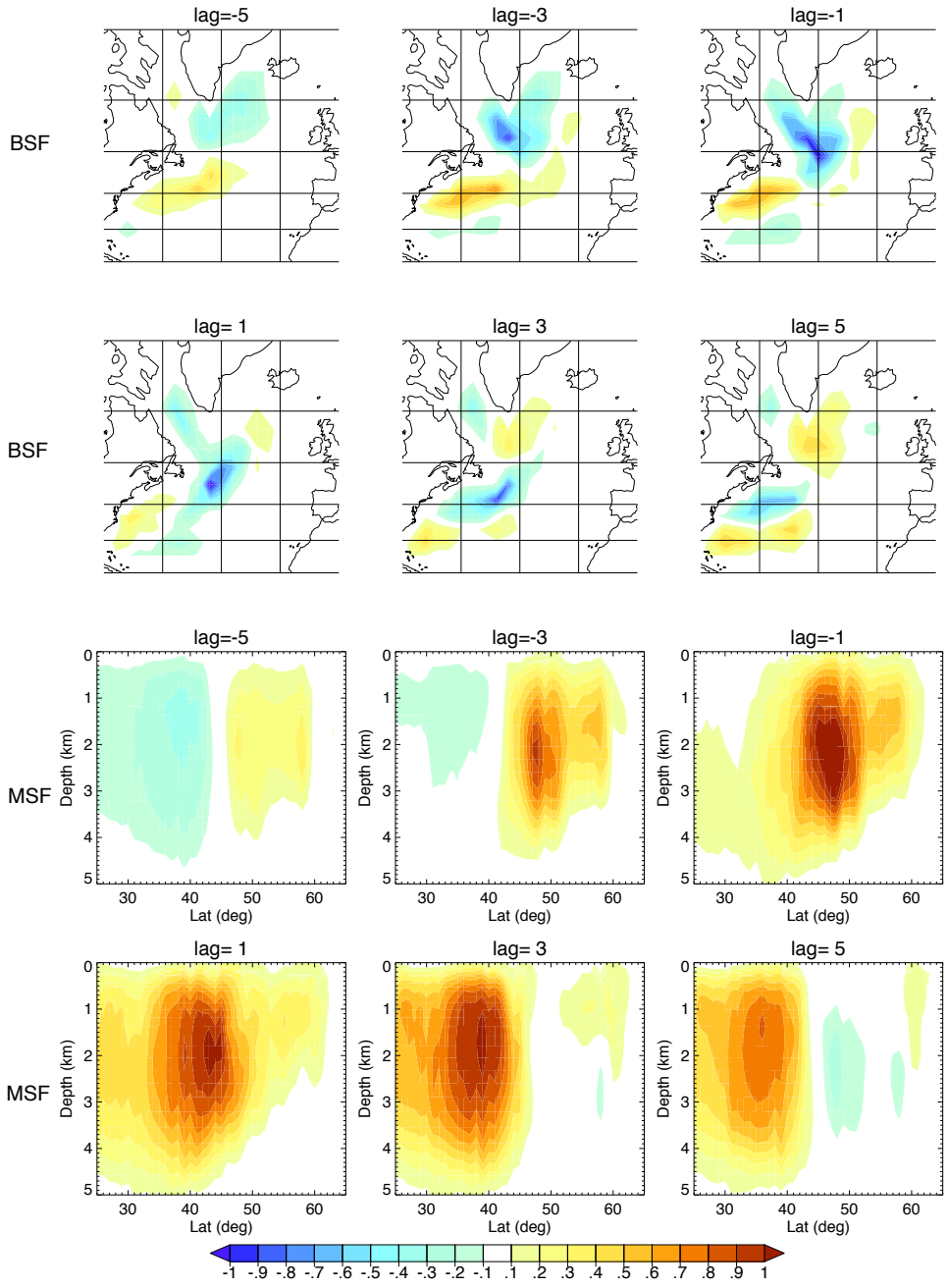

Figure 3.7. Regressions on 45°AMOC. The first two rows are for MSF; the last two rows are for BSF. Positive lag years mean 45°AMOC leads while negative lag years mean 45°AMOC lags.

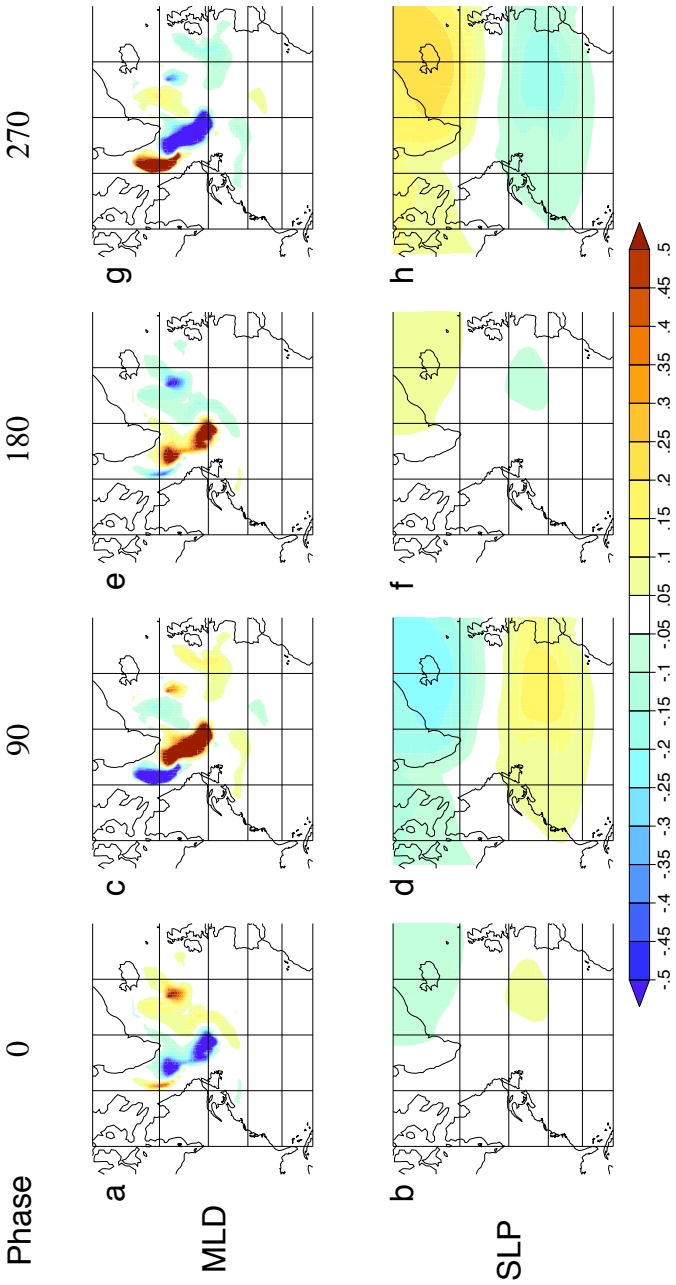

Figure 3.8. Associated correlation pattern (Eq. 2.11) of mixed layer depth and sea level pressure for Mode 2. The first row is for mixed layer depth (MLD), the second row is for sea level pressure (SLP).

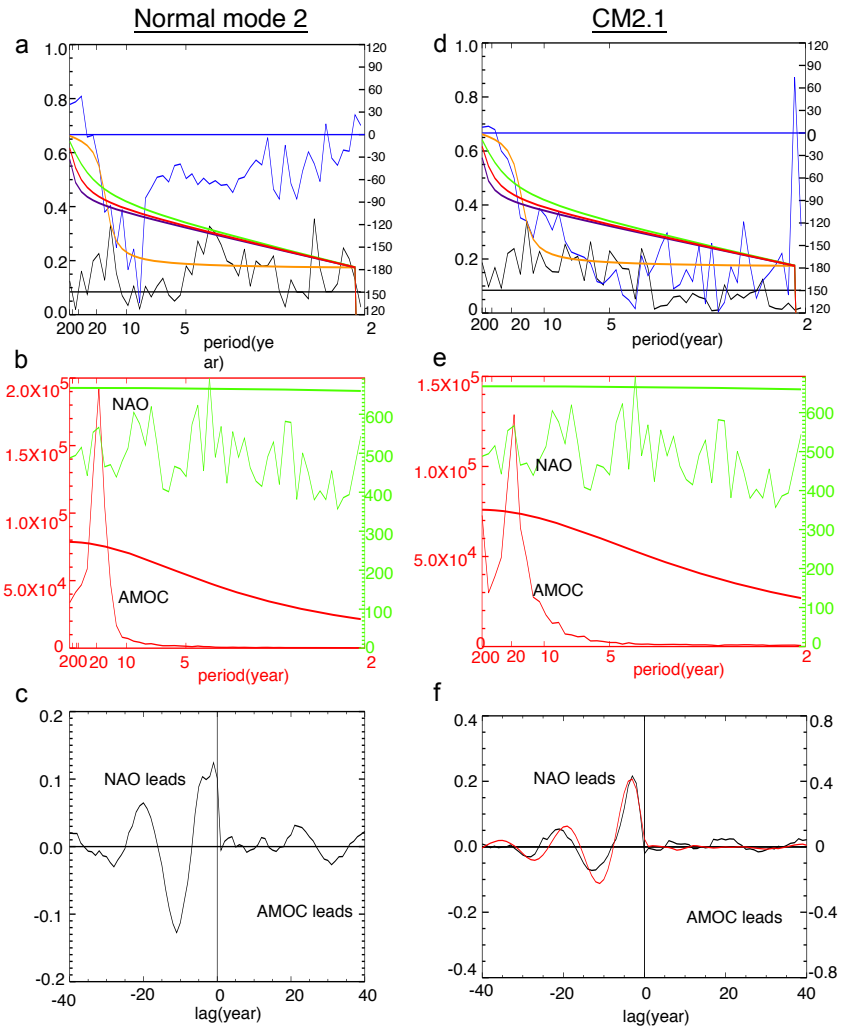

Figure 3.9. Spectral and correlation results for NAO and 45°AMOC. (a) Coherency and phase between NAO and 45°AMOC from Mode 2 alone. Thin black curve is the coherency while thick black curve is 95% significance level based on a F-test. Blue curve is the phase between 45°AMOC and NAO while orange curve is the fit to phase from linearly driven oscillator model and green, red and purple curves are fits to phase from delayed oscillator model with $\frac{cb}{\triangle t} = 5, 10, 20$, respectively. Parameters for linearly driven oscillator phase are determined from the GCM 45°AMOC time series (see text for details). (b) Red curve is the spectrum of 45°AMOC from Mode 2 while green curve is the NAO spectrum. Respective 95% significance levels based on a red noise null hypothesis and a χ^2-test are also shown by bold curves in corresponding colors. (c) Black curve is the cross-correlation between 45°AMOC from Mode 2 and NAO. Red curve is the cross-correlation between oscillator x and white forcing f. AMOC or x leads for positive lag years while NAO or f leads for negative lag years. (d-f) are similar to (a-c) except that 45°AMOC is from all normal modes, namely the GCM output.

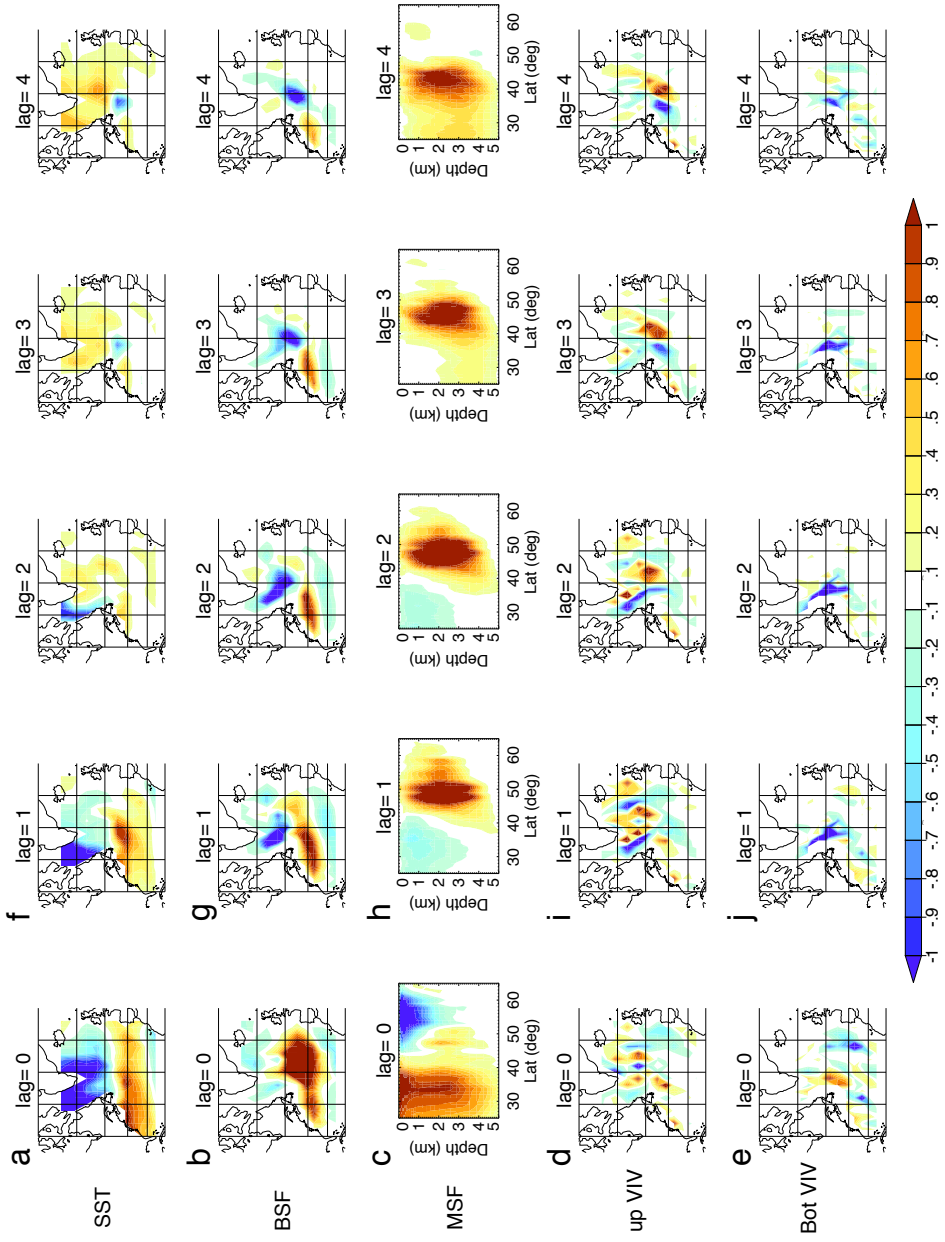

Figure 3.10. Regression onto NAO. The first row is for SST, second for BSF, third for MSF, fourth for upper level vertically integrated v-velocity (up VIV) and fifth for lower level vertically integrated v-velocity (bot VIV). From left to right, NAO leads from 0 to 4 years. Note that lag ≥ 1 year patterns differ markedly from the lag $= 0$ year pattern as discussed in the text.

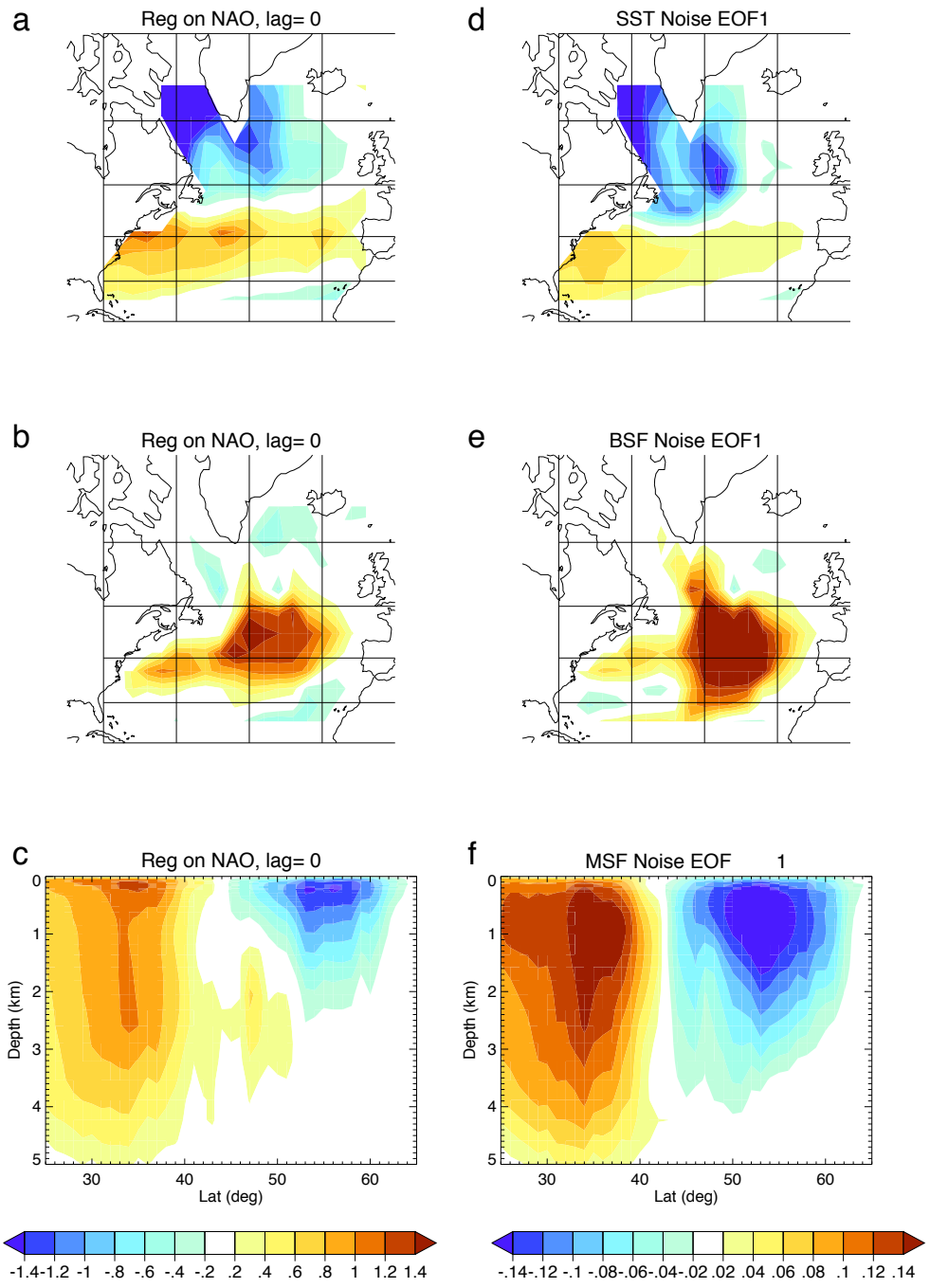

Figure 3.11. Comparison between NAO regression patterns and dominant noise patterns. (a-c) Regression patterns onto NAO at lat=0-year for (a) SST, (b) barotropic streamfunction and (c) meridional streamfnction. (d-f) First noise EOF patterns for (d) SST, (e) barotropic streamfunction and (f) meridional streamfunction.

CHAPTER 4

CONCLUSION

Utilizing the Linear Inverse Modelling (LIM), we have identified an interdecadal oscillatory mode of the North Atlantic atmosphere-ocean system that accounts for 20% of the SST-index variations (SST averaged over region [40°N, 60°N; 80°W, 30°W]) and 40% of the 45°AMOC variations. The mode is related to the interior pathway propagation of a high-latitude AMOC anomaly. Through spectral analysis, we have shown that this is an ocean-only mode excited by atmospheric forcing and in particular, that this mode can be approximately viewed as a linearly driven, underdamped oscillator with NAO providing at least part of the "external" forcing. By regressing streamfunctions and SSTs onto the NAO, we have seen evidence for a NAO-related wind stress forcing, but such influence quickly dies out and does not seem to be involved in an interdecadal oscillatory mode while AMOC-related deep ocean dynamics participate in the interdecadal oscillatory mode and account for most of the interdecadal variability. Therefore, this study calls attention to the role of ocean topography rather than surface wind stress alone in driving deep ocean variability, which then allows us to make decadal predictions of North Atlantic SSTs. The results of this study suggest that the North Atlantic atmosphere-ocean system can be summarized as follows: stochastic atmospheric forcing drives high-frequency SST variability directly through heat flux and wind stress; meanwhile, the atmosphere also drives low-frequency deep ocean current variability and hence indirectly induces low-frequency SST variability. It is thus the deep ocean component that prolongs SST predictability.

Due to the additive noise assumption in our LIM, we cannot examine the possible feedback from the ocean onto the atmosphere. On the other hand, since LIM is based on the linear assumption, most results shown here should be achievable with linearizing the vorticity equation, which is a goal of future work.

APPENDIX A

DETERMINATION OF γ AND ω_0

Consider $\zeta'' + \gamma\zeta' + \omega_0^2\zeta = 0$, where ζ is complex. Then $x = \Re(\zeta)$ and $x_H = \Im(\zeta)$, where x_H is the Hilbert Transform of x.

Let $y = \zeta'$, then $y' = -\gamma y - \omega_0^2\zeta$. Thus,

$$\frac{d}{dt}\begin{bmatrix}\zeta\\ y\end{bmatrix} = \begin{bmatrix}0 & 1\\ -\omega_0^2 & -\gamma\end{bmatrix}\begin{bmatrix}\zeta\\ y\end{bmatrix}. \tag{A.1}$$

The linear operator $\left[\begin{smallmatrix}0 & 1\\ -\omega_0^2 & -\gamma\end{smallmatrix}\right]$ has eigenvalues $\lambda_{1,2} = -\frac{\gamma}{2} \pm \frac{\mu}{2}i$ if $2\omega_0 > \gamma$, where $\mu = \sqrt{4\omega_0^2 - \gamma^2}$. Then the eigenvector $\boldsymbol{u_1}$ corresponding to $\lambda_1 = -\frac{1}{2}(\gamma - \mu i)$ is

$$\boldsymbol{u_1} = N_1\begin{bmatrix}1\\ -\frac{1}{2}(\gamma - \mu i)\end{bmatrix}, \tag{A.2}$$

where N_1 is a normalization constant. Similarly, the other eigenvector is

$$\boldsymbol{u_2} = N_2\begin{bmatrix}1\\ -\frac{1}{2}(\gamma + \mu i)\end{bmatrix}. \tag{A.3}$$

Therefore,

$$\begin{bmatrix}\zeta\\ \zeta'\end{bmatrix} = A_1' \cdot e^{-\frac{\gamma}{2}t + i\frac{\mu}{2}t} \cdot \boldsymbol{u_1} + A_2' \cdot e^{-\frac{\gamma}{2}t - i\frac{\mu}{2}t} \cdot \boldsymbol{u_2}, \tag{A.4}$$

and, absorbing the normalization constants into A_1' and A_2',

$$\begin{aligned}\zeta(t) &= A_1 \cdot e^{-\frac{\gamma}{2}t + i\frac{\mu}{2}t} + A_2 \cdot e^{-\frac{\gamma}{2}t - i\frac{\mu}{2}t}\\ &= (A_1 + A_2) \cdot e^{-\frac{\gamma}{2}t} \cdot \cos\left(\frac{\mu}{2}t\right) + (A_1 - A_2) \cdot e^{-\frac{\gamma}{2}t} \cdot \sin\left(\frac{\mu}{2}t\right) \cdot i\\ &= x(t) + \left(\frac{A_1 - A_2}{A_1 + A_2}\right) \cdot x_H(t) \cdot i.\end{aligned} \tag{A.5}$$

The preceding yields

$$\frac{d}{dt}\begin{bmatrix}x\\ x_H\end{bmatrix} = \begin{bmatrix}-\frac{\gamma}{2} & -\frac{\mu}{2}\\ \frac{\mu}{2} & -\frac{\gamma}{2}\end{bmatrix}\begin{bmatrix}x\\ x_H\end{bmatrix}. \tag{A.6}$$

The above operator can be determined by employing LIM and then used to derive γ and ω_0. For example,if x is 45°AMOC from GFDL CM2.1, LIM solves:

$$\begin{bmatrix}-\frac{\gamma}{2} & -\frac{\mu}{2}\\ \frac{\mu}{2} & -\frac{\gamma}{2}\end{bmatrix} = \begin{bmatrix}-2.4210505e^{-9} & -1.2410442e^{-8}\\ 1.2427851e^{-8} & -2.4513131e^{-9}\end{bmatrix} s^{-1}, \tag{A.7}$$

which yields $\gamma = 4.84e^{-9}s^{-1}$, $\omega_0 = 1.26e^{-8}$ or a decay time of 7 years and a period of 16 years. If x is 45°AMOC from Mode 2, LIM yields a decay time of 13 years and a period of 18 years.

APPENDIX B

PHASE OF DELAYED OSCILLATOR

Consider the phase lag between x and $\hat{f}$ as in

$$c\dot{x} = a\hat{f} - x/b.$$

Write the differential equation in finite difference form,

$$\hat{f}^n = \frac{c}{a\triangle t}(x^{n+1} - (1 - \frac{\triangle t}{cb}x^n), \tag{B.1}$$

where $\triangle t$ is the timestep and superscript denotes the time in the sense that $t = n\triangle t$. Take Fourier transform of the above equation and denote x's Fourier transform as as $\mathcal{F}(x)$ and x's complex conjugate as $x^\star$,

$$\mathcal{F}(\hat{f}) = \frac{c}{a\triangle t}(e^{i2\pi\omega} - (1 - \frac{\triangle t}{cb}))\mathcal{F}(x) \tag{B.2}$$

Denote cross-spectrum as $\Gamma_x f$,

$$\begin{aligned}\Gamma_{x\hat{f}} &= \mathcal{F}(x)\mathcal{F}(\hat{f})^\star \\ &= \frac{c}{a\triangle t}(e^{i2\pi\omega} - (1 - \frac{\triangle t}{cb}))\Gamma_{xx} \\ &= (\cos(2\pi\omega - i\sin(2\pi\omega) - (1 - \frac{\triangle t}{cb})))\frac{c}{a\triangle t}\Gamma_{xx}\end{aligned} \tag{B.3}$$

Therefore, the phase lag follows,

$$\Phi_{x\hat{f}} = \tan^{-1}(\frac{-sin(2\pi\omega)}{cos2\pi\omega - 1 + \frac{\triangle t}{cb}}). \tag{B.4}$$

Thus, $\Phi_{x\hat{f}}(\omega)$ is a function of only $\frac{cb}{\triangle t}$. Note that both the real and imaginary part of $\Gamma_{x\hat{f}}$ are negative, $\Phi_{x\hat{f}}$ should be in the range of $[-\frac{\pi}{2}, -\pi]$. $\frac{cb}{\triangle t}$ is actually the decay time of x in units of $\triangle t$. When x denotes oceanic variable, $\frac{cb}{\triangle t}$ should be much greater than 1. Hence,

$$\begin{aligned}\Phi_{x\hat{f}} &\approx \tan^{-1}(\frac{-sin(2\pi\omega)}{cos2\pi\omega - 1}) \\ \Phi_{x\hat{f}} &\approx \pi(0.5 - \omega).\end{aligned}$$

Fig. B.1 shows plot of $\Phi_{x\hat{f}}(\omega)$ for $\frac{cb}{\triangle t}$ equal to 5,10, 20, 50 and ∞.

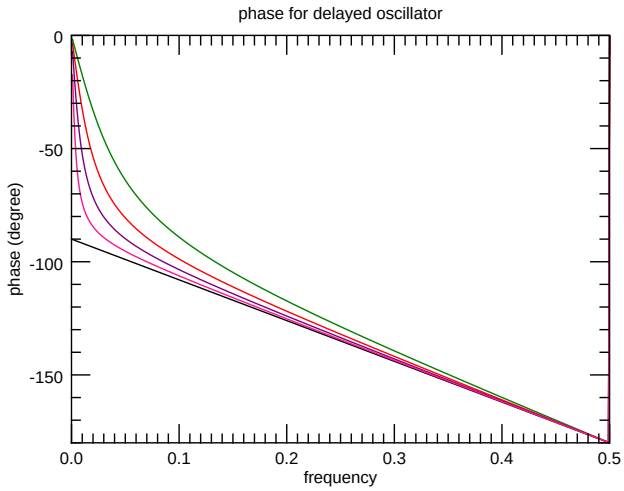

Figure B.1. Phase $\Phi_{x\hat{f}}(\omega)$ for different delay time. $\frac{cb}{\triangle t} = 5$ for green curve,$\frac{cb}{\triangle t} = 10$ for red curve, $\frac{cb}{\triangle t} = 20$ for purple curve, $\frac{cb}{\triangle t} = 50$ for dark pink curve, $\frac{cb}{\triangle t} = \infty$ for black curve.

APPENDIX C

REGRESSION ONTO AMOC

In Fig. C1, we show upper and lower level vertically integrated v-velocity regressed onto 45°AMOC as supplementary evidence for the consistency between ENM2/3 and AMOC-related velocity anomalies propagating equatorward.

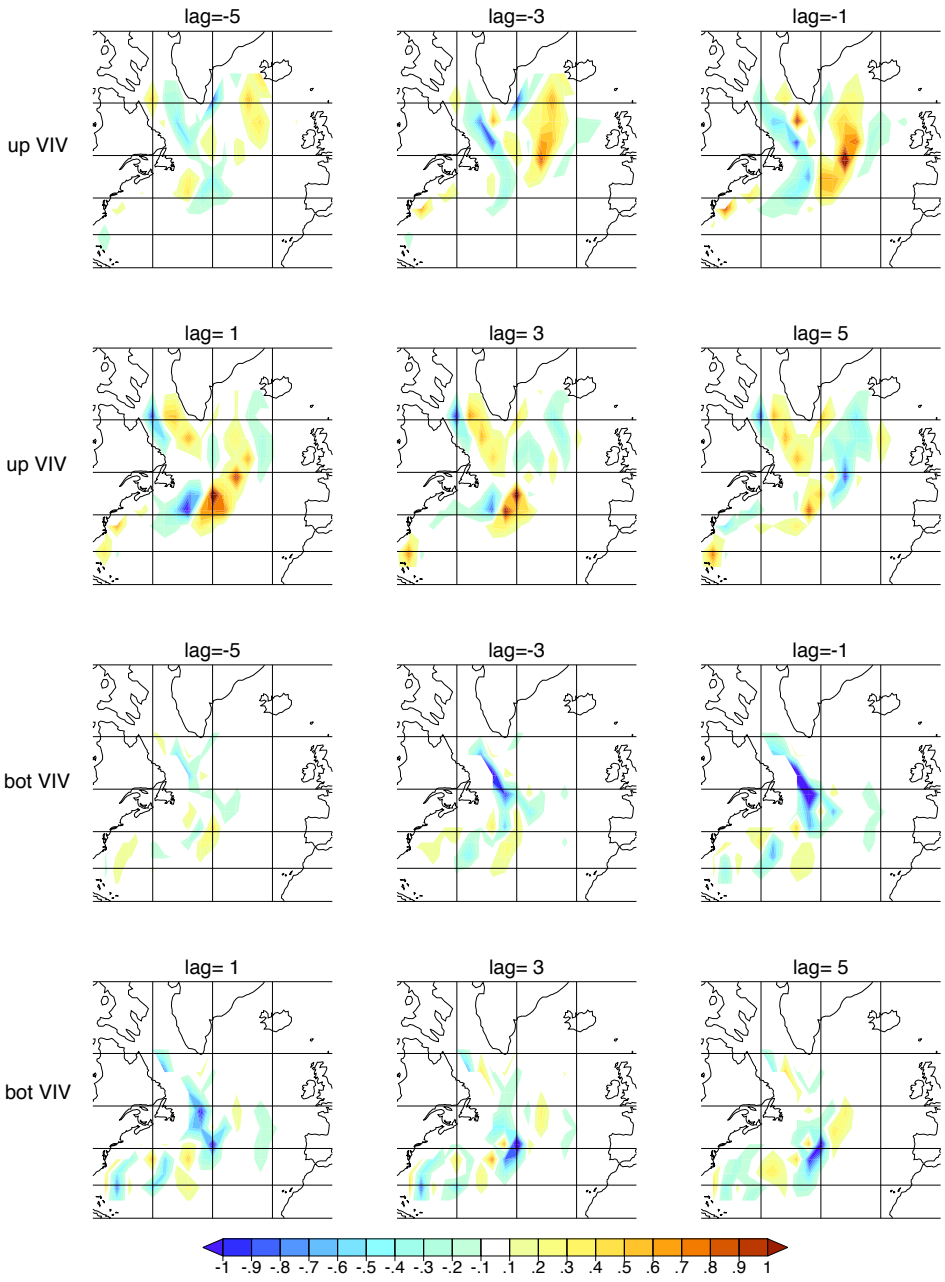

Figure C.1. Regression on 45°AMOC. The first two rows are for upper level vertically integrated v-velocity (up VIV); the last two rows are for lower level vertically integrated v-velocity (bot VIV). Positive lag years mean 45°AMOC leads while negative lag years mean 45°AMOC lags.

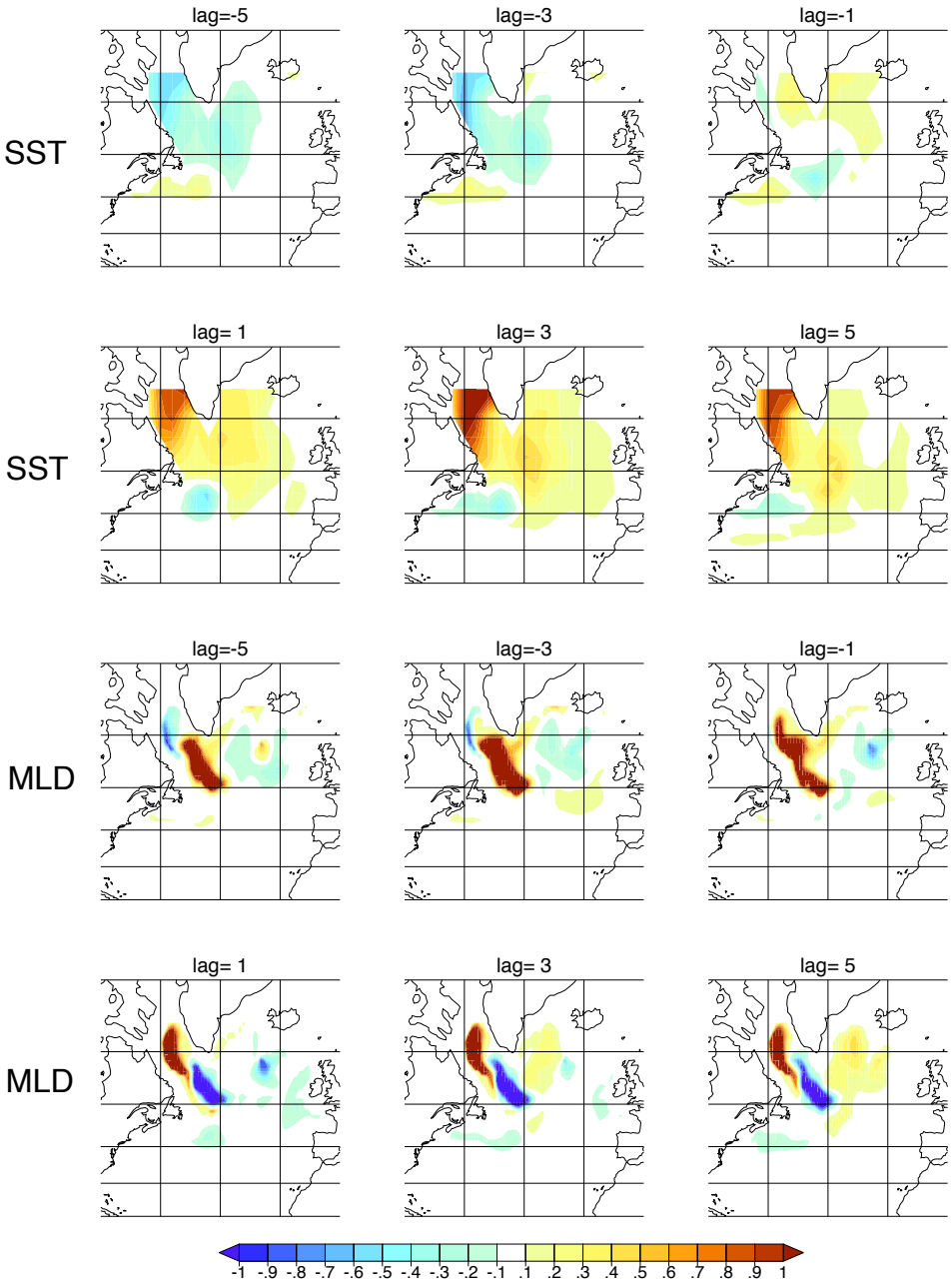

Figure C.2. Associated correlation pattern (Eq. 2.11) of SST and mixed layer depth for Mode 2. The first row is for SST, the second row is for mixed layer depth (MLD).

APPENDIX D

SPECTRAL RESULTS FOR DIFFERENT GFDL RUNS

In Fig. D1, we show spectral results for 45°AMOC and NAO that are from the concatenation of four different GFDL runs, each 4000 years in duration. The first one is the CM2.1 pre-industrial control run used in this paper. The second one is a CM2.1 present-day control run. The third is a present-day control run of CM2.1 with an extended stratosphere. The forth is a CM3 [38] control run. Note that the phase between AMOC and NAO agrees well with that between the oscillator x and white forcing f with $\frac{2\pi}{\omega_0} \approx 18$ years. Therefore, it is clear that the linear driven oscillator interpretation of AMOC is consistent across these different models. We also obtain similar results performing this analysis separately on each of the four runs.

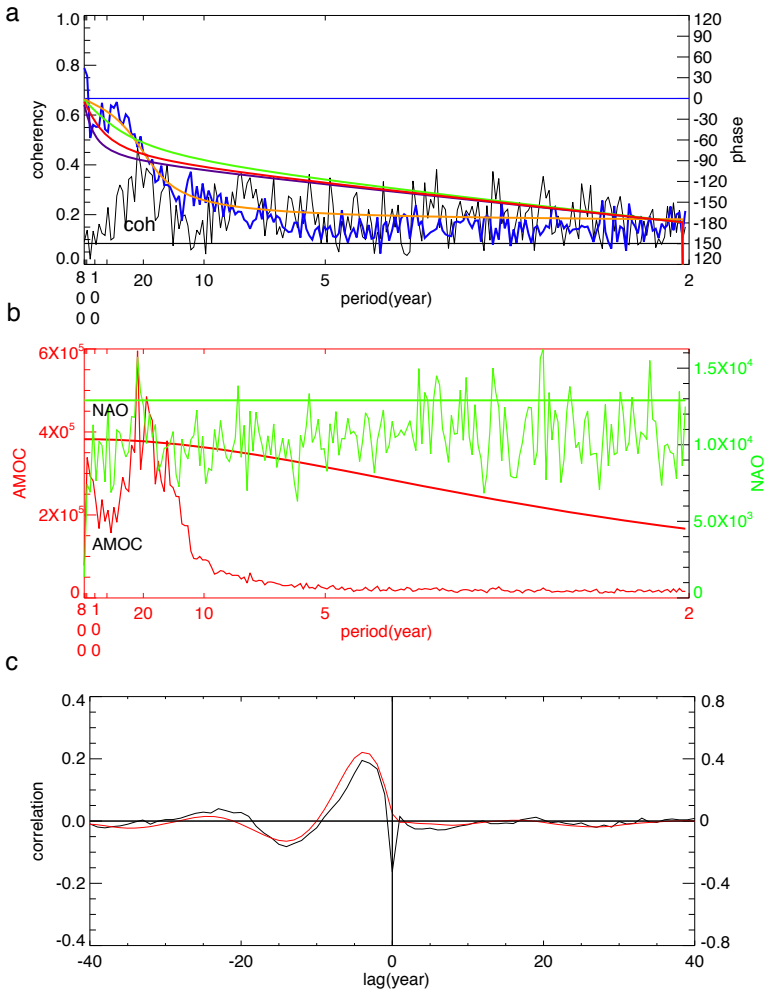

Figure D.1. Relationship between 45°AMOC and NAO from concatenation of four GFDL runs, each 4000 years in length.(a) Coherency and phase between 45°AMOC and NAO. Thin black curve is the coherency while thick black curve is 95% significance level based on a F-test. Blue curve is the phase between 45°AMOC and NAO while orange curve is the fit to phase from linearly driven oscillator model and green, red and purple curves are fits to phase from delayed oscillator model with $\frac{cb}{\triangle t} = 5, 10, 20$. Parameters for linearly driven oscillator phase are determined from the GCM 45°AMOC time series. (b) Red curve is the spectrum of 45°AMOC while green curve is the spectrum of NAO. Respective 95% significance levels based on a red noise null hypothesis and a χ^2-test are also shown by bold curves in corresponding colors. (c) Black curve is the cross-correlation between 45°AMOC and NAO. Red curve is the cross-correlation between oscillator x and white forcing f. Positive lag years mean AMOC or x leads while negative lag years mean NAO or f leads.

REFERENCES

[1] A. Czaja and C. Frankignoul, "Observed impact of atlantic sst anomalies on the north atlantic oscillation," *Journal of Climate*, vol. 15, no. 6, pp. 606–623, 2002.

[2] K. Hasselmann, "Stochastic climate models part i. theory," *Tellus*, vol. 28, no. 6, pp. 473–485, 1976.

[3] W. Weng and J. D. Neelin, "Analytical prototypes for ocean-atmosphere interaction at midlatitudes. part ii: Mechanisms for coupled gyre modes*," *Journal of Climate*, vol. 12, no. 9, pp. 2757–2774, 1999.

[4] J. D. Neelin and W. Weng, "Analytical prototypes for ocean-atmosphere interaction at midlatitudes. part i: Coupled feedbacks as a sea surface temperature dependent stochastic process*," *Journal of Climate*, vol. 12, no. 3, pp. 697–721, 1999.

[5] J. Marshall, H. Johnson, and J. Goodman, "A study of the interaction of the north atlantic oscillation with ocean circulation," *Journal of Climate*, vol. 14, no. 7, pp. 1399–1421, 2001.

[6] S. M. Griffies and E. Tziperman, "A linear thermohaline oscillator driven by stochastic atmospheric forcing," *arXiv preprint ao-sci/9502002*, 1995.

[7] T. L. Delworth and R. J. Greatbatch, "Multidecadal thermohaline circulation variability driven by atmospheric surface flux forcing," *Journal of Climate*, vol. 13, no. 9, pp. 1481–1495, 2000.

[8] C. Eden and J. Willebrand, "Mechanism of interannual to decadal variability of the north atlantic circulation," *Journal of Climate*, vol. 14, no. 10, pp. 2266–2280, 2001.

[9] S. Hkkinen, P. B. Rhines, and D. L. Worthen, "Atmospheric blocking and atlantic multidecadal ocean variability," *Science*, vol. 334, no. 6056, pp. 655–659, 2011.

[10] ——, "Northern north atlantic sea surface height and ocean heat content variability," *Journal of Geophysical Research: Oceans*, vol. 118, no. 7, pp. 3670–3678, 2013.

[11] R. Zhang and G. K. Vallis, "The role of bottom vortex stretching on the path of the north atlantic western boundary current and on the northern recirculation gyre," *Journal of Physical Oceanography*, vol. 37, no. 8, pp. 2053–2080, 2007.

[12] R. Zhang, "Latitudinal dependence of atlantic meridional overturning circulation (amoc) variations," *Geophysical Research Letters*, vol. 37, no. 16, pp. n/a–n/a, 2010.

[13] S. Yeager, "Topographic coupling of the atlantic overturning and gyre circulations," *Journal of Physical Oceanography*, vol. 45, no. 5, pp. 1258–1284, 2015.

[14] T. L. Delworth, A. J. Broccoli, A. Rosati, R. J. Stouffer, V. Balaji, J. A. Beesley, W. F. Cooke, K. W. Dixon, J. Dunne, and K. Dunne, "Gfdl's cm2 global coupled climate models. part i: Formulation and simulation characteristics," *Journal of Climate*, vol. 19, no. 5, pp. 643–674, 2006.

[15] E. Tziperman, L. Zanna, and C. Penland, "Nonnormal thermohaline circulation dynamics in a coupled oceanatmosphere gcm," *Journal of Physical Oceanography*, vol. 38, no. 3, pp. 588–604, 2008.

[16] E. Tziperman and P. J. Ioannou, "Transient growth and optimal excitation of thermohaline variability," *Journal of Physical Oceanography*, vol. 32, no. 12, pp. 3427–3435, 2002.

[17] L. Zanna and E. Tziperman, "Nonnormal amplification of the thermohaline circulation," *Journal of Physical Oceanography*, vol. 35, no. 9, pp. 1593–1605, 2005.

[18] E. Hawkins and R. Sutton, "Decadal predictability of the atlantic ocean in a coupled gcm: Forecast skill and optimal perturbations using linear inverse modeling," *Journal of Climate*, vol. 22, no. 14, pp. 3960–3978, 2009.

[19] L. Zanna, "Forecast skill and predictability of observed atlantic sea surface temperatures," *Journal of Climate*, vol. 25, no. 14, pp. 5047–5056, 2012.

[20] D. J. Vimont, "Analysis of the atlantic meridional mode using linear inverse modeling: Seasonality and regional influences," *Journal of Climate*, vol. 25, no. 4, pp. 1194–1212, 2012.

[21] F. Svellec and A. V. Fedorov, "The leading, interdecadal eigenmode of the atlantic meridional overturning circulation in a realistic ocean model," *Journal of Climate*, vol. 26, no. 7, pp. 2160–2183, 2013.

[22] C. Penland and P. D. Sardeshmukh, "The optimal growth of tropical sea surface temperature anomalies," *Journal of Climate*, vol. 8, no. 8, pp. 1999–2024, 1995.

[23] C. Penland and L. Matrosova, "A balance condition for stochastic numerical models with application to the el nino-southern oscillation," *Journal of Climate*, vol. 7, no. 9, pp. 1352–1372, 1994.

[24] M. Newman, M. A. Alexander, and J. D. Scott, "An empirical model of tropical ocean dynamics," *Climate Dynamics*, vol. 37, no. 9-10, pp. 1823–1841, 2011.

[25] H. von Storch, T. Bruns, I. Fischer-Bruns, and K. Hasselmann, "Principal oscillation pattern analysis of the 30- to 60-day oscillation in general circulation model equatorial troposphere," *Journal of Geophysical Research*, vol. 93, no. D9, p. 11022, 1988.

[26] H. von Storch, G. Brger, R. Schnur, and J.-S. von Storch, "Principal oscillation patterns: A review," *Journal of Climate*, vol. 8, no. 3, pp. 377–400, 1995.

[27] M. Newman and P. D. Sardeshmukh, "Tropical and stratospheric influences on extratropical short-term climate variability," *Journal of Climate*, vol. 21, no. 17, pp. 4326–4347, 2008.

[28] D. S. Battisti and A. C. Hirst, "Interannual variability in a tropical atmosphere-ocean model: Influence of the basic state, ocean geometry and nonlinearity," *Journal of the Atmospheric Sciences*, vol. 46, no. 12, pp. 1687–1712, 1989.

[29] J. R. Taylor, *Classical mechanics*. University Science Books, 2005.

[30] C. Sun, J. Li, and F.-F. Jin, "A delayed oscillator model for the quasi-periodic multidecadal variability of the nao," *Climate Dynamics*, vol. 45, no. 7-8, pp. 2083–2099, 2015.

[31] M. E. Mann and J. M. Lees, "Robust estimation of background noise and signal detection in climatic time series," *Climatic Change*, vol. 33, no. 3, pp. 409–445, 1996.

[32] K. Hasselmann, "Pips and pops: The reduction of complex dynamical systems using principal interaction and oscillation patterns," *Journal of Geophysical Research: Atmospheres*, vol. 93, no. D9, pp. 11 015–11 021, 1988.

[33] A. S. Bower, M. S. Lozier, S. F. Gary, and C. W. Böning, "Interior pathways of the north atlantic meridional overturning circulation," *Nature*, vol. 459, no. 7244, pp. 243–247, 2009.

[34] M. Kawase, "Establishment of deep ocean circulation driven by deep-water production," *Journal of Physical Oceanography*, vol. 17, no. 12, pp. 2294–2317, 1987.

[35] R. Zhang and G. K. Vallis, "Impact of great salinity anomalies on the low-frequency variability of the north atlantic climate," *Journal of Climate*, vol. 19, no. 3, pp. 470–482, 2006.

[36] D. R. Cayan, "Latent and sensible heat flux anomalies over the northern oceans: Driving the sea surface temperature," *Journal of Physical Oceanography*, vol. 22, no. 8, pp. 859–881, 1992.

[37] ——, "Latent and sensible heat flux anomalies over the northern oceans: The connection to monthly atmospheric circulation," *Journal of Climate*, vol. 5, no. 4, pp. 354–369, 1992.

[38] L. J. Donner, B. L. Wyman, R. S. Hemler, L. W. Horowitz, Y. Ming, M. Zhao, J.-C. Golaz, P. Ginoux, S.-J. Lin, and M. D. Schwarzkopf, "The dynamical core, physical parameterizations, and basic simulation characteristics of the atmospheric component am3 of the gfdl global coupled model cm3," *Journal of Climate*, vol. 24, no. 13, pp. 3484–3519, 2011.